cite as:
R. Gers, O Skurtys, N. I. Thiers, F. Moreau, D. Saury, "*Three-dimensional effects induced by depth variation in a differentially heated cavity*", Physics of Fluids, 34 (9), 093602, 2022.
DOI: 10.1063/5.0100218

Accepted to Phys. Fluids 10.1063/5.0100218

POF22-AR-02878

Three-dimensional effects induced by depth variation in a differentially heated cavity

R. Gers,[1] O. Skurtys,[2, a)] N. Thiers,[1] F. Moreau,[3] and D. Saury[3]

[1)]*Department of Mechanical Engineering, Universidad Técnica Federico Santa María, Avenida España 1680,Valparaíso ,Chile*

[2)]*Department of Mechanical Engineering, Universidad Técnica Federico Santa María, Av. Vicuña Mackenna 3939, Santiago ,Chile*

[3)]*Institut Pprime UPR CNRS 3346, CNRS – ENSMA – Université de Poitiers, Département FTC, Téléport 2, 1 Avenue Clément Ader, BP40109, F-86961 Futuroscope Cedex, France*

(*Electronic mail: didier.saury@ensma.fr)

(*Electronic mail: florian.moreau@ensma.fr)

(*Electronic mail: nicolas.thiers@usm.cl)

(*Electronic mail: olivier.skurtys@usm.cl)

(*Electronic mail: romain.gers@usm.cl)

(Dated: 1 August 2022)

Accepted to Phys. Fluids 10.1063/5.0100218

This work investigates a natural convection flow occurring in a differentially heated cavity. The main purpose of this paper is to analyze the influence of the cavity depth variation on heat transfers and flow dynamics. Three-dimensional numerical simulations are conducted. The working fluid is air, the vertical aspect ratio (cavity height over width) is equal to 4, and the Rayleigh Number is equal to 10^8. The impact of the rear and front boundary conditions on the flow topology are highlighted. When the cavity depth increases, three-dimensional effects are encountered that enhance local heat transfer at the isothermal walls. In particular, for horizontal aspect ratio (cavity depth over width) greater than 1, an alternation of local maximum and minimum Nusselt numbers can be observed along the *y*-direction toward the center of the wall in the lower half part of the isothermal wall, which are similar to a wave-like behavior. It is shown that they are due to vortex structures generated by a Görtler instability. The depth variation increases the emergence of those structures; but paradoxically several characteristics of both flow and heat transfer, such as the depth-averaged shear stress or the Nusselt numbers, tend to the two-dimensional case value as the cavity gets deeper.

[a)]Author to whom correspondence should be addressed: olivier.skurtys@usm.cl

Accepted to Phys. Fluids 10.1063/5.0100218

I. INTRODUCTION

Natural convection in a differentially heated cavity (DHC) has been the subject of intensive research in recent decades as these flows appear in many technical applications, like cooling of electronic equipment, solar collectors, air-conditioning, double pane windows and others. Even if the geometry is simple, buoyancy forces induced by local temperature gradients acting in a confined space can lead to complex flows. To understand the interactions between heat transfer and fluid dynamics various experimental or numerical investigations were carried out[1–6]. This configuration has served as a prototype for the development of numerical algorithms[7,8], to understand the onset of unsteadiness in fluid flows[9–14], or to establish rheological properties of fluids[15]. Many flow patterns are observed in vertical DHC depending on flow regimes, geometrical factors (vertical and horizontal aspect ratio), thermophysical properties of the convected fluid, temperature difference between walls[16], and top-bottom boundary conditions (adiabatic, conducting, or any intermediate possibility)[13,17–19]. However, due to the effects of radiation[20–23], water vapor content and uncertain thermal boundary conditions, it is still numerically difficult to reproduce the experimental flows[24].

Focussing on pure convection flow, the early numerical studies were performed in two-dimensional (2D) vertical square cavities where the flows is in the steady regime, *i.e.* the Rayleigh number $Ra \leq 10^8$ (see references[7,25]). In vertical DHC flows, beyond the critical Rayleigh number, flow and heat transfer become time-dependent (periodic, chaotic and eventually fully turbulent). Considering a vertical rectangular DHC filled with air, the transition is conduced by successive Hopf bifurcations resulting from traveling waves and instabilities in the vertical boundary layers. For a cavity with adiabatic horizontal walls and a vertical aspect ratio equal to 4 ($A_z = \frac{H}{W} = 4$ where H is the height of the cavity and W the width), Xin and Le Quéré[13] reported that the last Rayleigh number at which a steady-state solution is obtained is $Ra_H = 1.02 \times 10^8$. Most numerical studies about vertical DHC are performed under the assumption of a two-dimensional flow[25–28] or a three-dimensional case with front and rear periodic boundary conditions[18,19]. These conditions are often far from actual boundary conditions and could provide inconsistent solutions due to the influence of no-slip condition at the rear and front walls. Indeed, with periodic boundary conditions, even if the transverse velocity is one order of magnitude smaller than the vertical velocity in the boundary layers, a flow in the y-direction is observed if there is enough space in the periodic transverse direction[13]. So the 2D assumption should be used with caution. Thus, for

$A_z = 4$ considering a three-dimensional (3D) cavity with no-slip conditions applied to the vertical adiabatic walls (Dirichlet boundary conditions for the velocity components) could provide more realistic numerical results. However, to the best of our knowledge, for both laminar and turbulent regimes, only a few numerical results with no-slip boundary conditions on rear and front walls have been reported in the literature[21,29–31]. Furthermore, for a fixed vertical aspect ratio A_z and Rayleigh number Ra, it would be interesting to study the influence of adiabatic walls by varying the horizontal aspect ratio ($A_y = \frac{D}{W}$ where D is the depth of cavity) on the dynamic and thermal behavior of the flow. Indeed, a different flow behavior can be expected when the vertical adiabatic walls are close or far from each other.

The aim of this study is to improve our understanding of the dynamics of a natural convection flow in a differentially-heated cavity of vertical aspect ratio equal to 4 for a set of three-dimensional direct numerical simulations, considering that the horizontal aspect ratios A_y (depth over width) varies between 0.13 and 4.0 and a Rayleigh number based on the height of the cavity equal to 10^8. The boundary conditions on the vertical and horizontal walls are no-slip and adiabatic or isothermal. The present article is organized as follows: in Sec. II the studied problem, its modelling as well as a summary of the numerical methods used are presented. In Sec. III the numerical results obtained are exhibited. Finally, a physical explanation of the flow dynamics is presented in Sec. IV before giving concluding remarks in Sec. V.

II. PROBLEM FORMULATION AND NUMERICAL METHODS

Consider a three-dimensional differentially heated (DHC) cavity of height H, width W and depth D filled with air (assumed to be a Newtonian fluid) of kinematic viscosity ν, thermal diffusivity α, thermal expansion coefficient β and density ρ. The Prandtl number, $Pr = \frac{\nu}{\alpha}$ is supposed to be constant and equal to 0.71. The vertical aspect ratio $A_z = \frac{H}{W}$ is equal to 4. The two opposite vertical walls of the cavity (x-direction) are maintained at uniform but different temperatures T_{hot} at $x = 0$ and T_{cold} at $x = \frac{1}{A_z} = 0.25$. The gravitational acceleration $\vec{g}$ acts in the negative z-direction. A schematic view of the cavity is presented in Fig. 1a. Heat and fluid flows can be described by the unsteady Navier-Stokes equations under the Oberbeck-Boussinesq hypothesis. The Oberbeck-Boussinesq approximation ignores all density variations of the fluid in the governing equations, except when associated with the gravitational term. Using the temperature difference $\Delta T = T_{hot} - T_{cold}$ and the mean temperature $T_{mean} = \frac{T_{hot}+T_{cold}}{2}$, the reduced temperature θ can then

be defined as $\theta = \frac{T-T_{mean}}{\Delta T}$. Using the cavity height H as the reference length, the thermal diffusivity of air α and the Rayleigh number based on the cavity height $Ra = \frac{g\beta\Delta T H^3}{\alpha\nu}$, we define the reference velocity as $u_{ref} = \frac{\alpha}{H}\sqrt{Ra}$, the convection time $t_{ref} = \frac{H^2}{\alpha\sqrt{Ra}}$ and the reference pressure $P_{ref} = \rho u_{ref}^2$.

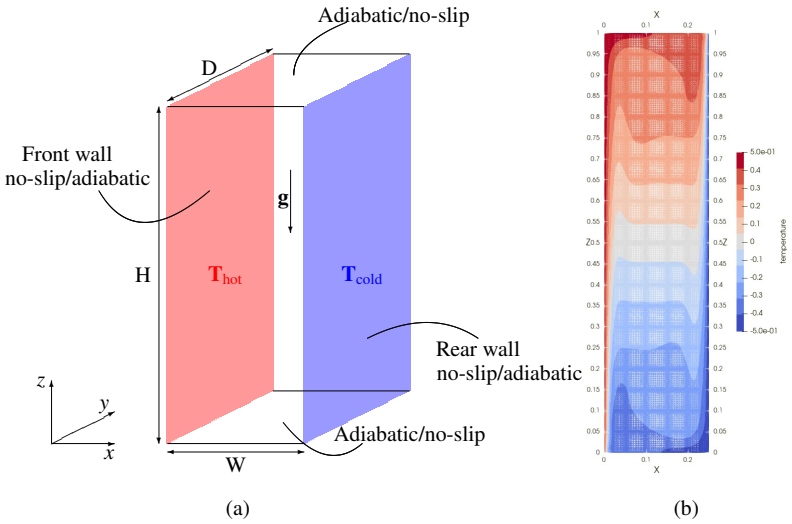

FIG. 1: a) Schematic diagram of the differentially heated cavity; b) The mesh in the xz-plane. An example of the temperature field is superimposed.

The dimensionless form of the Navier-Stokes equations under the Oberbeck-Boussinesq hypothesis yields:

$$\begin{cases} \frac{\partial u}{\partial x} + \frac{\partial v}{\partial u} + \frac{\partial w}{\partial z} = 0 \\ \frac{\partial u}{\partial t} + u\frac{\partial u}{\partial x} + v\frac{\partial u}{\partial x} + w\frac{\partial u}{\partial z} = -\frac{\partial p}{\partial x} + \frac{Pr}{\sqrt{Ra}}\left(\frac{\partial^2 u}{\partial x^2} + \frac{\partial^2 u}{\partial y^2} + \frac{\partial^2 u}{\partial z^2}\right) \\ \frac{\partial v}{\partial t} + u\frac{\partial v}{\partial x} + v\frac{\partial v}{\partial x} + w\frac{\partial v}{\partial z} = -\frac{\partial p}{\partial y} + \frac{Pr}{\sqrt{Ra}}\left(\frac{\partial^2 v}{\partial x^2} + \frac{\partial^2 v}{\partial y^2} + \frac{\partial^2 v}{\partial z^2}\right) \\ \frac{\partial w}{\partial t} + u\frac{\partial w}{\partial x} + v\frac{\partial w}{\partial x} + w\frac{\partial w}{\partial z} = -\frac{\partial p}{\partial z} + \frac{Pr}{\sqrt{Ra}}\left(\frac{\partial^2 w}{\partial x^2} + \frac{\partial^2 w}{\partial y^2} + \frac{\partial^2 w}{\partial z^2}\right) + \mathrm{Pr}\theta \\ \frac{\partial \theta}{\partial t} + u\frac{\partial \theta}{\partial x} + v\frac{\partial \theta}{\partial y} + w\frac{\partial \theta}{\partial z} = \frac{1}{\sqrt{Ra}}\left(\frac{\partial^2 \theta}{\partial x^2} + \frac{\partial^2 \theta}{\partial y^2} + \frac{\partial^2 \theta}{\partial z^2}\right) \end{cases} \quad (1)$$

where (x, y, z) are non-dimensional coordinates, t the non-dimensional time, and (u, v, w) are the velocity components in respectively x, y and z directions. As the Prandtl number Pr and the vertical aspect ratio $A_z = \frac{H}{W}$ are fixed, the solution of the equations is only dependent on

the Rayleigh number Ra and the horizontal aspect ratio $A_y = \frac{D}{W}$. In the present study, vertical cavity of vertical aspect ratio $A_z = 4$ is chosen because the 3D critical Rayleigh numbers and the structures of the unstable modes are similar to those observed in the 2D case. Indeed, Xin and Le Quéré [13] showed that the last Rayleigh number at which a steady-state solution is obtained is $Ra = 1.02 \times 10^8$. The influence of the horizontal aspect ratio A_y which varies between 0.13 and 4.0 (i.e. $0.13W \leq D \leq 4W$) for $Ra = 10^8$ is explored in the present work. At such a Rayleigh number, the flow should be in a steady state since the value of the Rayleigh number is slightly lower than the critical value to reach instationnarity. Vertical isothermal walls are held at imposed uniform temperatures $\theta(x = 0, y, z) = \theta_{hot} = 0.5$ and $\theta(x = \frac{1}{A_z}, y, z) = \theta_{cold} = -0.5$, respectively. The top and bottom walls ($z = 0$ and $z = 1$) as well as the front and rear walls ($y = 0$ and $y = A_y/4$) are adiabatic (the Neumann boundary condition is $\frac{\partial \theta}{\partial n} = 0$). Finally, on the six walls, the velocity field satisfies the no-slip condition: $u = v = w = 0$. Initial velocities are set to zero in all directions. Initial temperature values are usually a linear conduction profile (in the x direction) ranging from $\theta = 0.5$ to $\theta = -0.5$. For simulations that take an extended time to find a steady state (especially for higher A_y), the initial conditions are set to a settled state from a previous simulation for a lower Rayleigh number (with the same aspect ratio).

The system of equations (1) is solved by the computational fluid dynamics open-source program Nek5000 developed and maintained by Paul Fischer[32] at the Argonne National Laboratory. Nek5000 is a Navier-Stokes solver, which uses a spectral element method proposed by Patera[33], to accurately resolve the velocity field $\vec{u}(x, y, z, t)$ and temperature field $\theta(x, y, z, t)$. This method combines the benefits of high-order spectral methods with finite element methods. The computational domain is made of $N_x \times N_y \times N_z$ hexahedral spectral elements, in the x, y and z-directions, respectively. On each spectral element, the Navier-Stokes equations (see Eq. 1) are rewritten in the weak formulation and discretized by a Galerkin method, where test and trial functions are sought in different polynomial spaces. Indeed, a $\mathbb{P}_N - \mathbb{P}_{N-2}$ formulation is used: the velocity and temperature fields are discretized using Nth degree Lagrange interpolants, defined on the Gauss-Lobatto-Legendre (GLL) quadrature points, as basis and trial functions, while the pressure field is discretized using Lagrange interpolants of degree $N - 2$ defined on the Gauss-Legendre quadrature points. The time-derivative terms are discretized by the third-order backward differentiation formula (BDF3). The nonlinear convective terms are computed explicitly using a third-order extrapolation scheme (EXT3), while the linear terms are treated implicitly. This high-order splitting method (BDF3-EXT3) leads to a Poisson equation for pressure and Helmholtz equations for tem-

perature and velocity components that are solved using a generalized minimal residual method (GMRES) where the tolerance is set to 10^{-8}. More details on the numerical scheme and appropriate grid resolution can be found in Fischer et al.[34]. The spatial resolution is selected using as a guideline, the mesh reported in Trias *et al.* [18] for $Ra = 6.4 \times 10^8$ ($N_x \times N_y \times N_z = 156 \times 128 \times 312$ for $A_y = 2$). In the streamwise and spanwise directions, the distribution of spectral elements is chosen uniform, while to obtain a well refined mesh near the isothermal walls, spectral elements $(E_x)_j$ in the x-direction are distributed using a hyperbolic-tangent function:

$$(E_x)_j = \frac{1}{8}\left(1 + \frac{\tanh\left[\gamma_x\left(\frac{2(j-1)}{N_x} - 1\right)\right]}{\tanh\gamma_x}\right) \tag{2}$$

where γ_x is the concentration parameter fixed to 2.5. E_x and E_z are fixed to 7 and 20 respectively (see Fig. 1b) while N_y varies with A_y according to the following relationship:

$$\begin{cases} E_y = A_y \times 5 + 2 \quad \text{if} \quad A_y \geq 0.1 \\ E_y = 3 \quad \text{if} \quad A_y < 0.1 \end{cases} \tag{3}$$

Thus, N_y ranges from 3 to 22. A mesh convergence study was performed using a p-refinement technique in which the grid polynomial order N was increased: $N = 22, 24, 26$. It has been shown that $N = 24$ is sufficient to obtain an accurate Nusselt number at the isothermal wall and that increasing the polynomial order does not affect the simulation results. For $A_y = 2$, $N_x \times N_y \times N_z = 168 \times 288 \times 480$ gives a better resolution than the mesh reported in Trias *et al.* [18] for a higher Rayleigh number. We have also checked that the cold and hot Nusselt numbers are equal. Thus, close to the isothermal walls, the smallest wall-normal distance is $\frac{(\Delta x)_{min}}{H} = 1.3 \times 10^{-4}$. A constant time-stepping with a target Courant-Friedrichs-Lewy number of 0.25 is used, which is in practice more than sufficient to guarantee the stability during the simulation. Each calculation is extended until the flow reaches a steady stage.

III. NUMERICAL RESULTS AND DISCUSSIONS

A. A reference case: the square based DHC ($A_y = 1$)

The horizontal aspect ratio, $A_y = 1$ (i.e. $D = W$), is firstly chosen as a reference case because several experimental[2,35,36] and numerical[13] data (temperature and velocity fields) are available. For this geometry, steady flow is considered with a fixed Rayleigh number $Ra = 10^8$ just below

the first critical Rayleigh number. To identify and visualize flow structures, and in particular the vortex-dominated regions, the Q criterion is used. It was defined by Jeong and Hussain[37] as:

$$Q = \frac{1}{2}\left(\Omega_{ij}\Omega_{ij} - S_{ij}S_{ij}\right) \tag{4}$$

where $\Omega_{ij} = (u_{i,j} - u_{j,i})/2$ and $S_{ij} = (u_{i,j} + u_{j,i})/2$ are respectively the antisymmetric and symmetric components of velocity gradient tensor. In other words, Q is the balance between the rotation rate $\Omega^2 = \Omega_{ij}\Omega_{ij}$ and the strain rate $\mathbf{S}^2 = S_{ij}S_{ij}$. Thus, the rotation motion dominates for isosurfaces where $Q > 0$, while the deformation motion dominates for isosurfaces where $Q < 0$. Therefore, the isosurface $Q = 0$ represents the boundary of the region in which the rotation rate dominates.

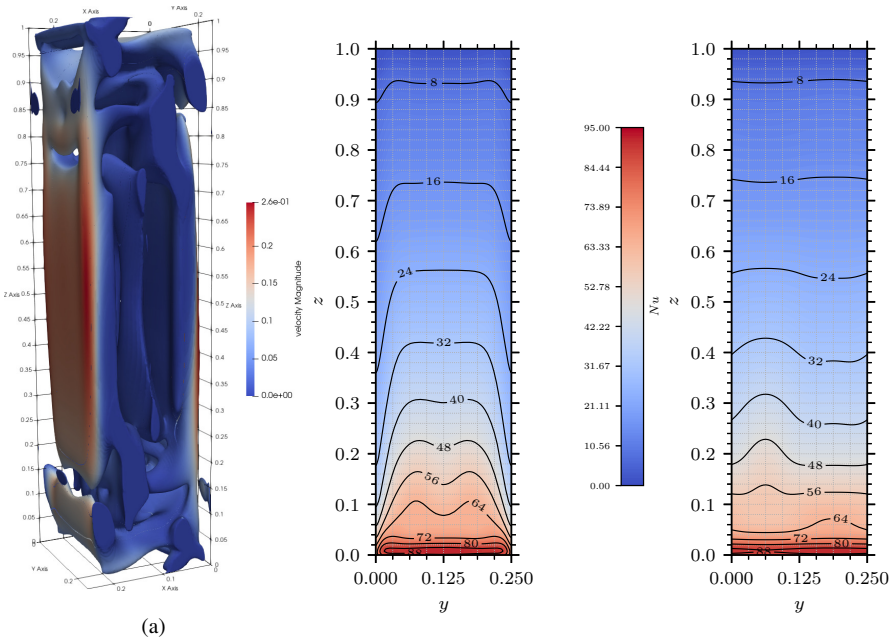

(a) (b) wall BC (c) periodic BC

FIG. 2: For a square based cavity $A_y = 1$: a) the isosurfaces $Q = 0$ are colored by the magnitude of velocity; b) local Nusselt number, Nu, at the hot wall for front and rear no-slip boundary conditions; c) idem as b) but for front and rear periodic BCs.

Figure 2a shows the isosurface $Q = 0$ colored by the magnitude of velocity. The following characteristics can be observed: the vertical boundary layers are connected by horizontal flows which take place along the top and bottom walls; the core of the cavity remains motionless; recirculation cells can be distinguished at the bottom and top part of the cavity. In addition, two velocity peaks are also present in the vertical edges between the hot wall and the rear and front walls, respectively. For natural convection flows, as the coupling between temperature and velocity fields is strong, the dynamic boundary conditions have a fundamental influence on the velocity fields but also on the temperature fields. To highlight the influence of the fluid dynamics on heat transfer, the local Nusselt number, $Nu = -\frac{\partial \theta}{\partial x}(x = 0, y, z)$, calculated at the hot wall is presented in Fig. 2b. It is clear that Nu is not constant with respect to y. The maximum values of the Nusselt numbers are located at the bottom of the hot wall (red area); this is due to the cold air coming from the cold wall and impacting the hot wall. Nusselt numbers are more uniform in the central and upper half part of the wall ($z \in [0.5; 1]$). However, the rear and front walls play a significant role not only on the flow structures but also on the heat flux at the isothermal walls: for a constant z, the Nusselt numbers are lower close to the adiabatic rear and front walls, and the heat transfer is predominant in the central part of the hot wall. In Fig. 2c, the Nusselt number at the hot wall is presented for front and rear periodic boundary conditions. Clearly, these periodic boundary conditions in the $y-$direction significantly modify the spatial distribution of the heat flux at the isothermal walls. This phenomenon was mentioned by Xin and Le Quéré [13] for a Rayleigh number greater than 2.141×10^7. Indeed, if there is enough space in the periodic $y-$direction, a flow in the $y-$direction is observed where v velocity is one order of magnitude smaller than u and w velocities.

Although there are many experimental studies on natural convection in air-filled cavities, it can be stressed that those works have only reported velocity and temperature fields in the mid-plane which is a plane of symmetry[2,36]. Indeed, experimentally it is very difficult to measure 3D fields in the whole cavity[38]. In Fig. 3a, the horizontal profiles of the time-averaged vertical velocity $\langle w \rangle$ are measured by Laser Doppler Anemometry (LDA) along the y-direction in planes $x = 0.0125$ and $x = 0.2375$ (see Skurtys [35]). Note that this cavity is not a perfectly square based cavity since $A_y = 1.167$. In order to check whether there is any dissymmetry between the profiles, we have superimposed the profiles for each of the isothermal walls. Due to center-symmetry, the values for the cold wall are related to the measured values for the hot wall: $w(x, y, z) \longleftrightarrow -w(\frac{1}{A_z} - x, y, 1 - z)$. It can also be seen that each profile of the vertical velocity has 3 maxima (two close to the adiabatic walls and one in the central part), and 2 minima. The vertical plane $y = 0.146$ is a plane of

symmetry for the vertical component of the velocity; in this plane the absolute value of w reaches its maximum. In Fig. 3b our numerical results for the horizontal profiles of the vertical velocity w perpendicular to the adiabatic wall ($x = 0.0125$) are presented for the square based cavity. For each height, two maxima near the adiabatic walls are also found. However the central velocity is less prominent, this could be explained by wall radiation effects[21,23] that are not encountered in our simulations, and by a slightly different horizontal aspect ratio. Indeed, experimentally the front and rear walls are made of polycarbonate, they are opaque for infrared and have thus strong emissivities[35]. As very few numerical results including radiative effects are available in the literature, to facilitate comparison between our results and those of other authors these effects are not accounted for in our simulations.

Finally, since numerical results obtained with periodic conditions in the $y-$direction may not be compared with experimental results, all results presented in the next section are obtained with no-slip boundary conditions at all cavity faces.

Accepted to Phys. Fluids 10.1063/5.0100218

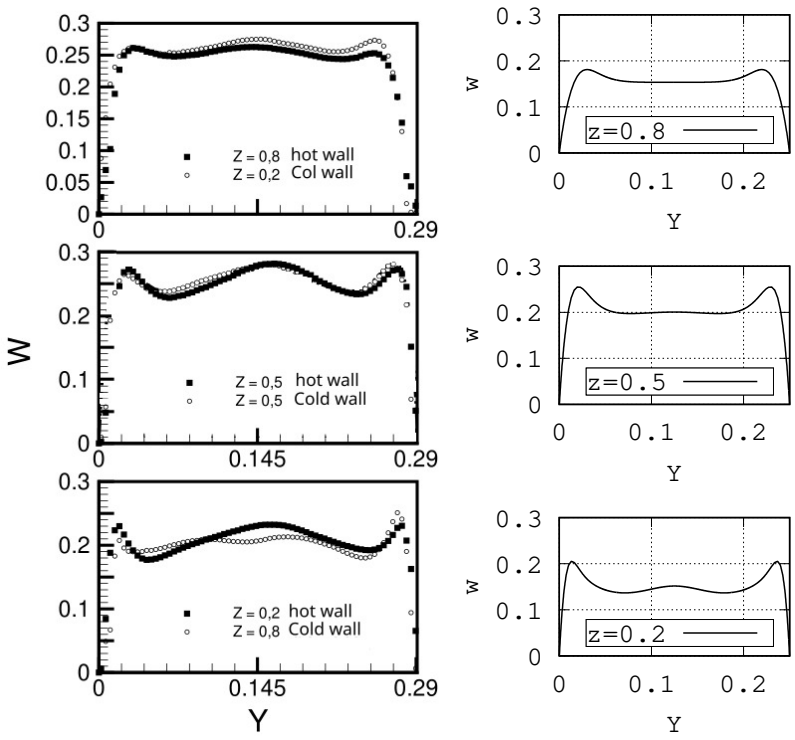

(a) (b)

FIG. 3: For Ra $= 10^8$, a) Experimental results of Skurtys[35]. Horizontal profiles of the time-averaged vertical velocity W measured by LDA along the y-direction for three different heights z. Comparison between the cold wall ($x = 0.2375$) and the hot wall ($x = 0.0125$); $A_z = 4$, $A_y = 1.167$; b) our numerical results of horizontal profiles of the vertical velocity w perpendicular to the adiabatic walls ($x = 0.0125$) for three heights z, $A_z = 4$, $A_y = 1$.

B. Effect of the horizontal aspect ratio A_y on the heat transfer and the flow

In this section, we present in detail the effects of the horizontal aspect ratio, which varies from 0.13 to 4, first on the heat transfer, and in a second part on the flow dynamics.

1. Heat transfer

The spatially-averaged Nusselt number $\langle Nu \rangle$ at the hot wall, i.e. the global heat transfer is first investigated. It is calculated by:

$$\langle \mathrm{Nu}_{3D}(A_y) \rangle = \frac{4}{A_y} \int_0^1 \int_0^{A_y/4} -\frac{\partial \theta}{\partial x}(x=0,y,z)\, dy\, dz \tag{5}$$

The values of the averaged Nusselt number (Eq. 5) are gathered in Table I for different horizontal aspect ratio A_y. It can be seen in this table that $\langle \mathrm{Nu}_{3D}(A_y) \rangle$ increases from 25.01 (*i.e.* $A_y = 0.13$) to 30.72 ($A_y = 4$) when A_y increases. It also seems that values tend to approach a finite constant value corresponding to the Nusselt numbers calculated for a 2D cavity $\langle \mathrm{Nu}_{2D} \rangle$ which corresponds to $A_y \to \infty$. The values of Table I can be fitted by the following equation:

$$\langle \mathrm{Nu}_{3D}(A_y) \rangle = \langle \mathrm{Nu}_{2D} \rangle \left(\frac{-0.024}{A_y} + 1 \right), \qquad R^2 = 0.9975 \tag{6}$$

where R^2 is the coefficient of determination. To more clearly illustrate the trend of the averaged Nusselt number to converge towards the 2D value as A_y increases, Fig. 4 plots the evolution of the 3D Nusselt number $\langle \mathrm{Nu}_{3D}(A_y) \rangle$ divided by the 2D Nusselt number $\langle \mathrm{Nu}_{2D} \rangle$ according to A_y. This plot confirms that $\dfrac{\langle \mathrm{Nu}_{3D}(A_y) \rangle}{\langle \mathrm{Nu}_{2D} \rangle}$ tends asymptotically to 1.

TABLE I: Values of the averaged Nusselt number $\langle \mathrm{Nu}_{3D}(A_y) \rangle$ at the isothermal wall according to the horizontal aspect ratio A_y. The last column reports its value in the 2D configuration[39].

A_y	0.13	0.2	0.3	0.4	0.6	0.8	1	2	3	4	∞ (2D)
$\langle Nu_{3D}(A_y) \rangle$	25.01	27.21	28.36	29.04	29.66	29.88	30.04	30.41	30.50	30.56	30.72

The fact that $\langle \mathrm{Nu}_{3D} \rangle$ tends to $\langle \mathrm{Nu}_{2D} \rangle$ can be linked with the ratio of total isothermal to total adiabatic surface. The total isothermal surface S_T^{3D} is the sum of the surface of the hot wall and the surface of the cold wall, that is to say: $S_T^{3D} = 2 \times (H \times D)$. The total adiabatic surface S_Q^{3D} refers to the sum of the surfaces of the bottom, the top, the rear and front of the cavity, that is to say: $S_Q^{3D} = 2 \times (H \times W) + 2 \times (W \times D)$. So the ratio of total isothermal to total adiabatic surface in the 3D configuration gives:

$$\frac{S_T^{3D}}{S_Q^{3D}} = \frac{HD}{HW + WD} = \frac{1}{\frac{1}{A_y} + \frac{1}{A_z}} \tag{7}$$

Accepted to Phys. Fluids 10.1063/5.0100218

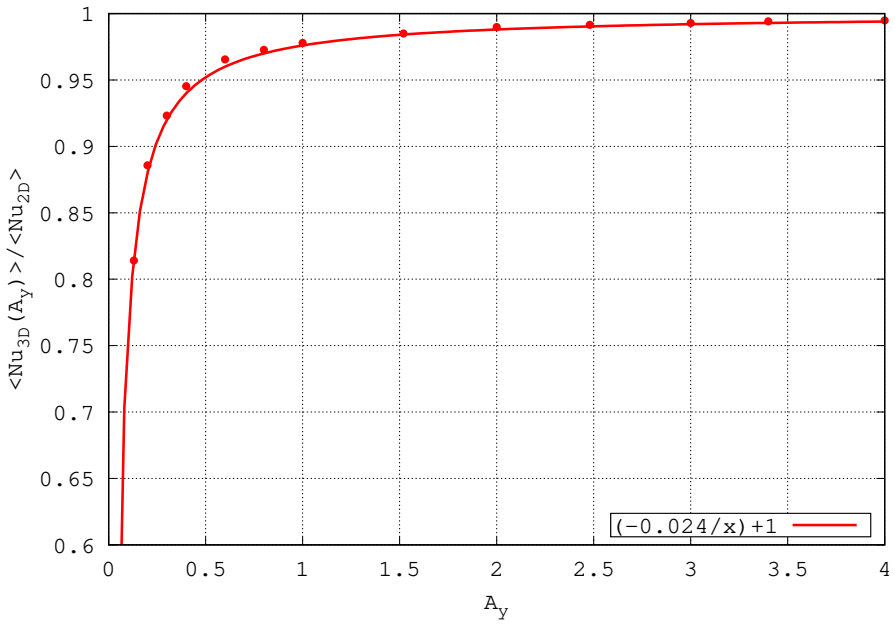

FIG. 4: Evolution of $\frac{\langle \mathrm{Nu}_{3D}(A_y)\rangle}{\langle \mathrm{Nu}_{2D}\rangle}$ according to the horizontal aspect ratio A_y. A best-fit curve to these data points is also plotted.

while in the 2D case it is equal to $\frac{S_T^{2D}}{S_Q^{2D}} = \frac{H}{W} = A_z$. Indeed, the total isothermal surface S_T^{2D} and the total adiabatic surface S_Q^{2D} for the 2D cavity are respectively: $S_T^{2D} = 2 \times H$ and $S_Q^{2D} = 2 \times W$. As a consequence, as the horizontal aspect ratio A_y tends to infinity, we have:

$$\lim_{A_y \to +\infty} \left(\frac{S_T^{3D}}{S_Q^{3D}} \right) \mapsto A_z = \frac{S_T^{2D}}{S_Q^{2D}} \tag{8}$$

This calculation confirms that the 3D averaged Nusselt number should tend to the 2D value even if 3D structures could influence the Nusselt number patterns.

After presenting the Nusselt number averaged in y and z, we focus now on its dependence on z. Figure 5a presents the profiles of the Nusselt number averaged in y, $\langle Nu(A_y,z)\rangle_y = \frac{4}{A_y}\int_0^{A_y/4} Nu(x=0,y,z)\,dy$, versus the cavity height z, for $Ra = 10^8$ and various A_y values (0.3, 1, 2, 4). For all curves, the highest Nusselt number, about 90, is close to the bottom of the hot wall because this wall is impacted by the cold air coming from the cold wall. As the air ascends

all along the hot wall, it gets heated. As a consequence, the Nusselt number decreases when z increases. Except for $z \in [0.05; 0.1]$ (see Fig. 5a), we observe again that, as the horizontal aspect ratio increases from $A_y = 0.3$ (doted black line) to $A_y = 4$ (red line), the mean values of the Nusselt number tends to approach those of the 2D profile (black line).

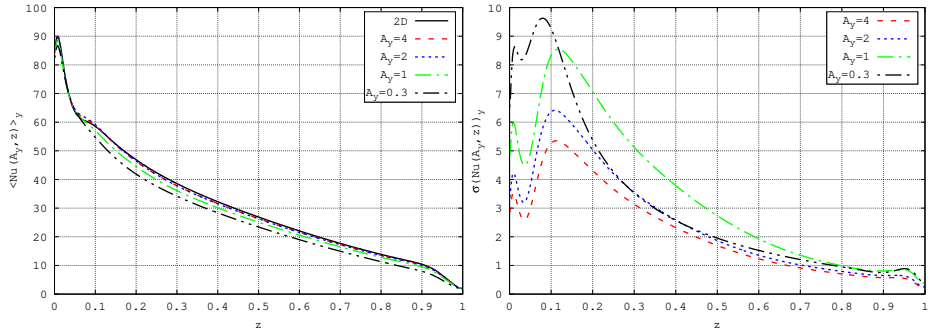

(a) (b)

FIG. 5: For various horizontal aspect ratios A_y values: a) profiles of spatially-averaged Nusselt number $\langle Nu(A_y,z)\rangle_y$ (in the y-direction) in the plane $x = 0$ versus the cavity height z. The two-dimensional case is also presented for comparison; b) spatial standard deviations of $Nu(A_y)$ (*i.e.* $\sigma(Nu(A_y,z))_y$) versus z.

Now, it is interesting to study how the y-averaged profile of the Nusselt number is representative of the Nusselt number profiles at each $y-$position. Figure 5b shows the spatial standard deviations calculated from all the mesh points along the $y-$direction. We first see that the major deviations occur at the bottom of the hot wall in all cases, that is to say for $z \in [0; 0.2]$ whatever the value of A_y. Besides, higher deviation values are achieved when the cavity is flatter *i.e.* A_y decreases. It could appear paradoxical: indeed, 3D effects should be more important as A_y increases but the local y-averaged-Nusselt number fits better and better to the 2D profile when A_y increases. This trend is concurrent with evolution of the global Nusselt number observed previously. To better understand this behavior, Figs. 6a-6g display the fields of local Nusselt numbers $Nu(x = 0, y, z)$ at the hot wall and a cavity ratio A_y ranging from 0.3 to 4.

We can note in Figs. 6a-6g that, once again, the maximum values of the local Nusselt number are at the bottom of the hot wall (red areas). In the lower part of the hot wall ($z \in [0; 0.5]$), an alternation of local maximum and minimum Nusselt numbers can be observed along the y-

Accepted to Phys. Fluids 10.1063/5.0100218

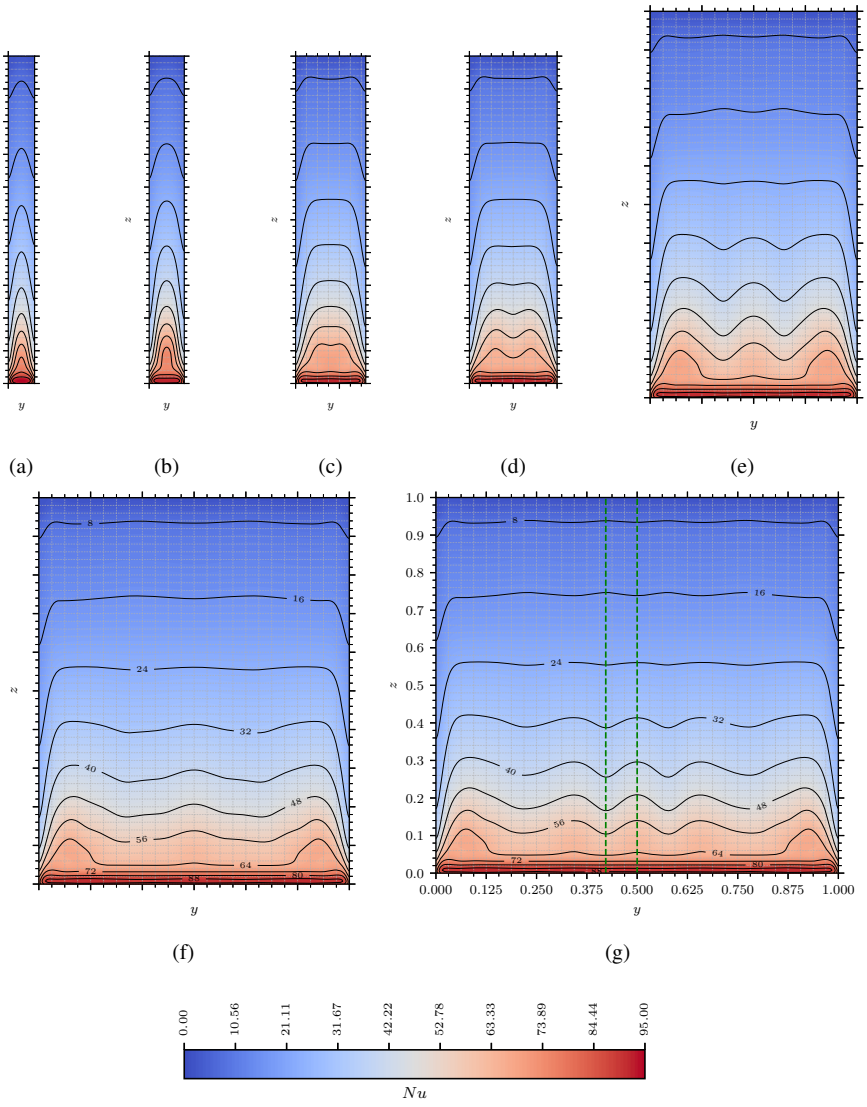

FIG. 6: Effect of the horizontal aspect ratio A_y on the local Nusselt number, Nu, at the hot wall. Both dashed green lines are helpful in visualizing the Nusselt behavior along the hot wall: a) $A_y = 0.3$, b) $A_y = 0.4$, c) $A_y = 0.8$, d) $A_y = 1$, e) $A_y = 2$, f) $A_y = 3$, g) $A_y = 4$.

direction toward the center of the wall, which are similar to a wave-like behavior (black contour lines). We will explain in the next section which phenomenon is responsible for these heat transfer disparities. In the upper half wall ($z \in [0.5;1]$), Nusselt numbers are more uniform. Indeed, Figs. 6a-6g show that the local Nusselt numbers are higher close to the adiabatic rear and front walls (for $y \in [0;\frac{1}{2A_y}] \bigcup [A_y - \frac{1}{2A_y};A_y]$) when A_y is large enough ($A_y \geq 1$). These fields explain why the 3D Nusselt number averaged in space tends to the 2D value: at the center of the hot wall, heat transfer is more homogeneous as the horizontal aspect ratio A_y increases; as a consequence, the weight of the reduced heat transfer in the corners with the rear or front walls in the averaging process of the Nusselt number is reduced. That is why, in Fig. 5b, the spatial standard deviations of $Nu(A_y)$, $\sigma(Nu(A_y,z))_y$, increases when A_y diminishes. Finally, it is important to note that, even if a flow in the y-direction is observed ($\mathrm{Ra} > 2.141 \times 10^7$, see Xin and Le Quéré [13]) all fields stay symmetric about $y = A_y/8$.

To end the presentation of the effect of the horizontal aspect ratio A_y on the heat transfer, it is also necessary to present temperature profiles far from the isothermal walls in detail. Figure 7 shows the vertical profile of the y-averaged temperature, $\langle \theta(A_y,z) \rangle_y = \frac{4}{A_y} \int_0^{A_y/4} \theta\left(x = \frac{A_y}{2}, y, z\right) dy$ for four different A_y values, in the mid-width plane $x = \frac{A_x}{2}$ versus the cavity height z. The 2D profile is added to complete the analysis. We observe that for $z \in [0.25;0.75]$, all profiles are quite identical. They exhibit a linear behavior at the center part with a usual slope equal to 1 (see Xin and Le Quéré [11], Trias *et al.* [28]). Differences appear at the top ($z \geq 0.75$), and at the bottom of the cavity ($z \leq 0.25$). This may be due to a modification of the velocity profile in the boundary layer of the main velocity loop. This aspect could easily be investigated but that this is not the focus of the paper. Moreover, it again seems to be case that, as the cavity depth increases, the y-averaged vertical profile of temperature tends to approach the 2D profile (solid line)..

To sum up this part, an increase of the horizontal aspect ratio A_y induces an increase of the Nusselt number which tends to the value obtained in a 2D DHC. Furthermore a decrease of A_y reveals spatial inhomogeneities of the heat transfer at the isothermal walls. We will explain those inhomogeneities in the next section through a dynamics analysis of the flow.

2. *Flow dynamics*

In order to explain the wavy patterns of the Nusselt number fields at the bottom of the hot wall (see Figs. 6a-6g), the main flow structures are highlighted by iso-surfaces of $\sqrt{{\omega_x}^2 + {\omega_z}^2}$

Accepted to Phys. Fluids 10.1063/5.0100218

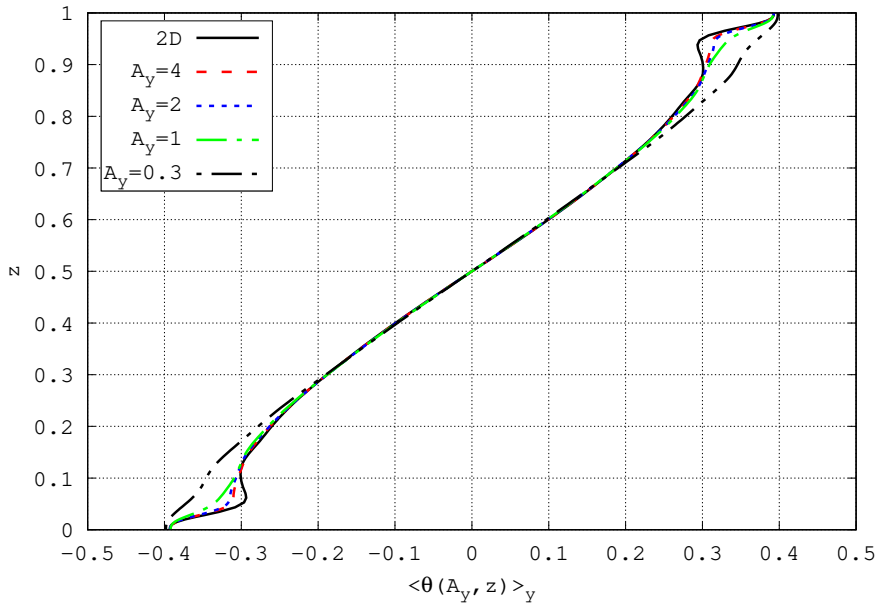

FIG. 7: For various horizontal aspect ratios A_y (0.3, 1, 2, 4), vertical profile of the y-averaged temperature $\langle\theta(A_y,z)\rangle_y$ in the mid-width plane $x=\frac{A_x}{2}$ versus the cavity height z. The two-dimensional case is also presented for comparison.

colored by the horizontal velocity component, v, where ω_x and ω_z refers respectively to the x and z-component of the vorticity (see Figs. 8a-8d).

Two kinds of structures have to be distinguished: structures along the vertical edges between the isothermal walls and the adiabatic rear or front face, and more central structures at the top or the bottom of the DHC whose axes are aligned with the main flow direction. The first kind of structure corresponds to vortices which have the form of tori along the edges of the vertical adiabatic wall, that is to say turning between planes parallel to the (x,z) plane. The second kind of structures are only apparent when the primary flow changes its direction from the top or bottom face of the DHC to the isothermal wall. This alternation of central structures explains the wave-like contour lines observed in the Nusselt number fields presented before in Figs. 6a-6g . This phenomenon may be explained by a Görtler instability at the bottom of the hot plate, and at the top of the cold wall, which generates vortices when the flow changes its direction from the horizontal

Accepted to Phys. Fluids 10.1063/5.0100218

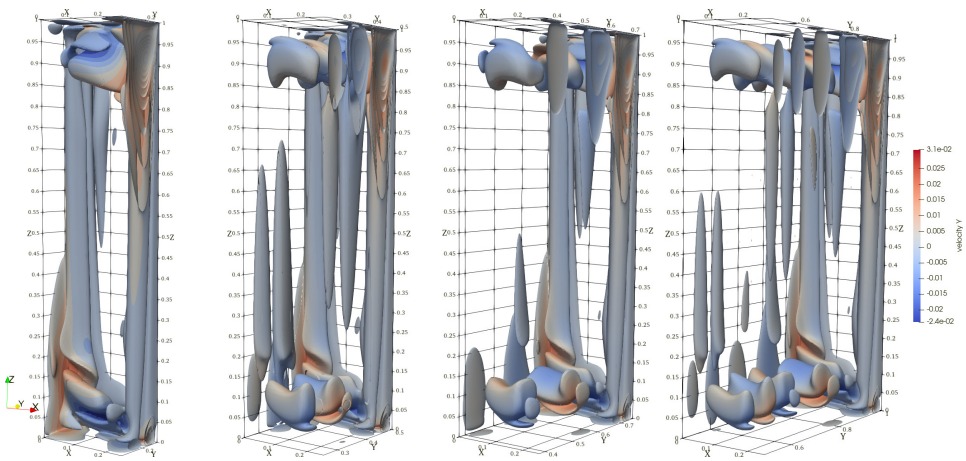

(a) (b) (c) (d)

FIG. 8: For various horizontal aspect ratios A_y, iso-surfaces of $\sqrt{\omega_x{}^2+\omega_z{}^2}=0$, 0.5, 1, 1.5, 2, 2.5, 3, 3.5, 4. The horizontal velocity component, v, is superimposed: a) $A_y=1$, b) $A_y=2$, c) $A_y=3$, d) $A_y=4$. The left wall corresponds to the hot wall. Only the mid-depth cavity is shown ($y\in[\frac{A_y}{2};A_y]$) to highlight the flow structures.

to the vertical plane (see section IV). At the top of the hot plate, these structures probably keep existing as they still have an influence on the local Nusselt number (see Figs. 6a-6g) but possibly with a lower intensity and a more complex structure. Indeed, these vortices gradually dissipate along the vertical walls, on the one hand, since there is no longer any centrifugal force present, and on the other hand since they are subjected to the buoyancy force. That is why, isovalue lines of the Nusselt number in Figs. 6a-6g are quite horizontal in the top half part of the hot plate. Moreover, observing a vertical line at the hot wall, it can be noted that a maximum of an isovalue line of Nusselt numbers at the bottom of the hot plate becomes a minimum at the upper part of the plate, and vice versa when the horizontal aspect ratio is large enough (see vertical green dashed lines in Fig. 6g).

Now we detail these structures through the presentation of the horizontal velocity component v first in the vertical plane of equation $x=\frac{W}{2}$ for several values of A_y (see Figs. 9a-9g), and secondly in various horizontal planes of equation $z=\{0.1,0.3,0.5\}$ for $A_y=2$ (see Fig. 10c). Figures 9a-9g shows that the number of structures depends on the depth A_y and confirms that two

kinds of vortices can be distinguished. Indeed, we observe that, up to $A_y = 1$, it is possible to see only two main vortices which stay in the corner joining the vertical isothermal and adiabatic walls (probably Ekman or Eckhaus like vortex, see section IV). Their size, referred as λ_c, increases from $A_y = 0.3$ to $A_y = 1$ so that $\lambda_c = \frac{A_y}{4}$. For deeper cavities ($A_y > 1$), they seem to reach a maximal size since λ_c is a constant: $\lambda_c = 0.219$. This observation for deeper cavities has to be linked with the presence of a variable number of new structures between the corner vortices. For $A_y = 2$, we can note four secondary structures between them. When the depth is multiplied by two, that is to say for $A_y = 4$, the number of secondary structures is multiplied by two again. These structures are pairs of counter-rotating vortices, whose rotation seems to be imposed by the rotation of the corner vortices which have an higher y-velocity (see Fig. 10c) and a less dissipated structure along the z-direction (see Figs. 8a-8d). The reduction of kinetic energy of both vortex types can be observed with increasing z, which is certainly due to the lack of a centrifugal force, but vortex stretching due to the buoyancy force can also contribute to the gradual dissipation of the Görtler vortices and the weakening of the corner vortex.

Now, the two-way coupling between those vortices and the heat transfer, has to be described. We can speak of a two-way coupling because vortices are generated by the convection flow, provoked itself by the temperature difference between the isothermal walls, and at the same time, these vortices influence the heat transfer. To detail this influence, the analysis of the heat transfer at the bottom half-part of the hot plate has to be separated from the analysis at the top half-part of the hot plate because the mechanisms are different. At the bottom half-part of the hot plate, the interaction between fluid dynamics and heat transfer seems to work as follows (see Fig. 10a): cold air from the cavity core is transported towards the hot wall due to the angular velocity. The peaks in the Nusselt number distribution coincide with the stagnation points of this secondary flow. On the contrary, when both adjacent angular velocities suck hot air from the plate, the Nusselt number decreases. That is why the Nusselt number fields appear in a wavy form. Besides, Fig. 10a shows an horizontal distribution of the Nusselt number which could depend on the fluid acceleration which can be deduced from the distances between two streamlines and which also correlates to the wall shear stress magnitude peak (see Fig. 10b). Peaks of Nusselt number seem to correspond to a lower vertical velocity (see Fig. 10c) or a lower mass flow rate (the distance between streamlines increases), the minimum to a higher vertical velocity or a higher mass flow rate (the distance between streamlines decreases). This might lead to the paradoxical conclusion that the vertical flow velocity and the local Nusselt number are inversely related, and that this would ex-

Accepted to Phys. Fluids 10.1063/5.0100218

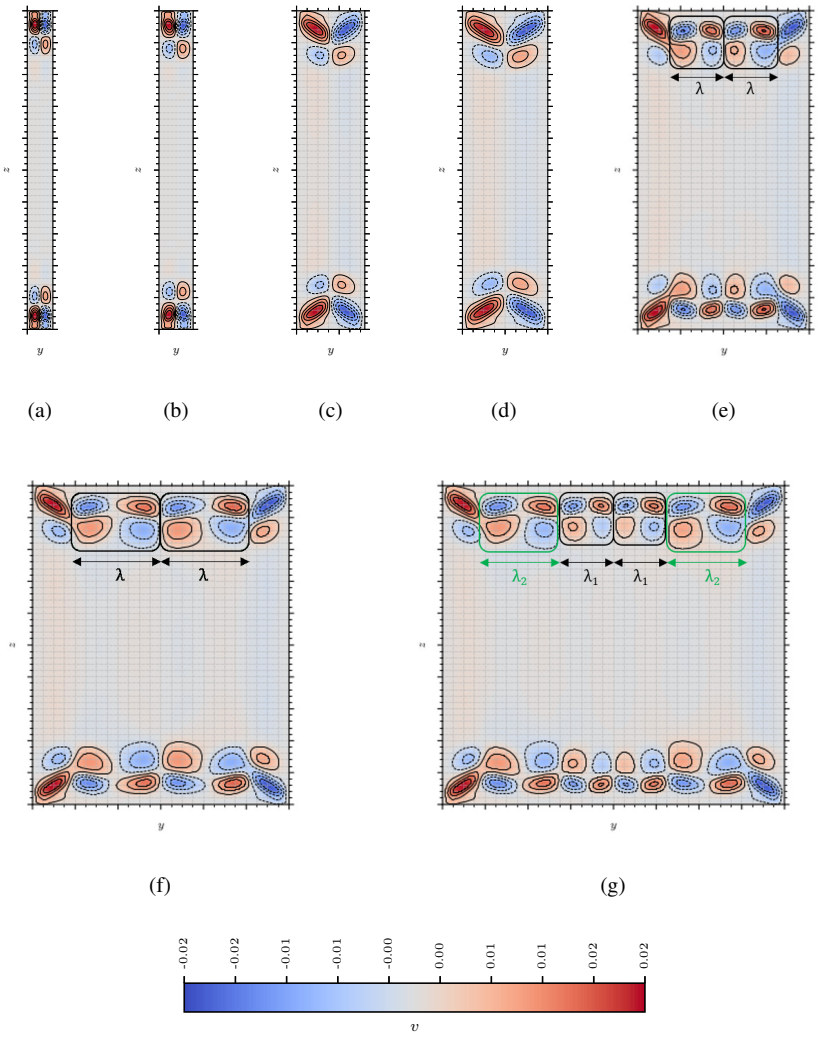

FIG. 9: For various horizontal aspect ratios A_y, the horizontal velocity v in the vertical mid-width plane $x = \frac{W}{2}$: a) $A_y = 0.3$, b) $A_y = 0.4$, c) $A_y = 0.8$, d) $A_y = 1$, e) $A_y = 2$, f) $A_y = 3$, g) $A_y = 4$. The wavelengths of the vortices are: a-d) $\lambda_c = \frac{A_y}{4}$ e) $\lambda = 0,141$; f) $\lambda = 0,265$; g) $\lambda_1 = 0,141$, $\lambda_2 = 0,234$.

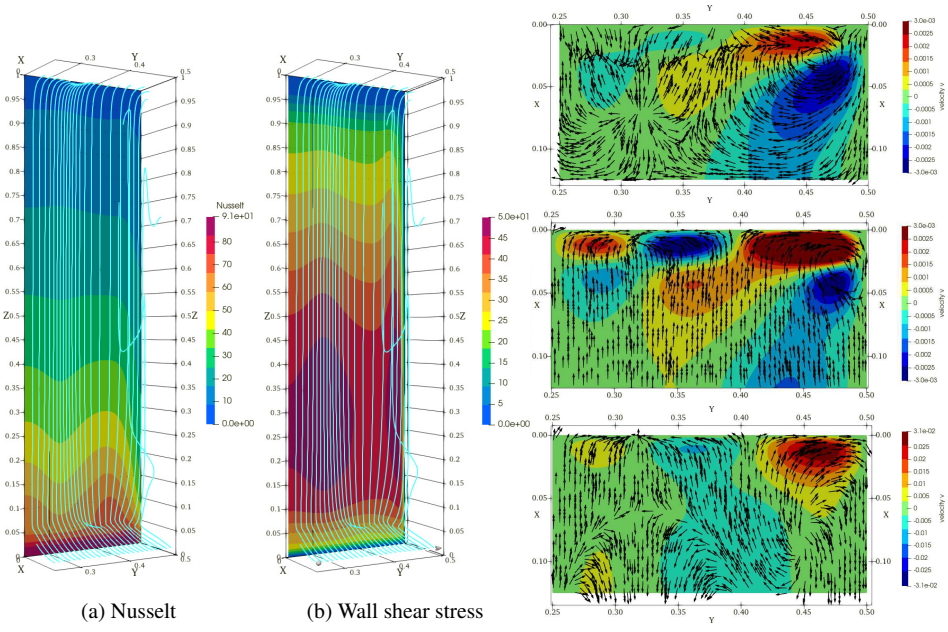

(a) Nusselt (b) Wall shear stress (c)

FIG. 10: For $A_y = 2$, a) streamlines and local Nusselt number along the hot wall; b) wall shear stress magnitude, $WSSmag = \sqrt{\sigma_{zx}^2 + \sigma_{yx}^2}$, along the hot wall; c) in various horizontal planes of equation $z = \{0.1, 0.3, 0.5\}$, the y-velocity component v and the velocity vector fields are also shown. Only the region $x \geq 0.125$ and $y \geq 0.25$ is presented.

plain the wavy form of the Nusselt number isovalue lines. However, the authors are convinced that the secondary flow is responsible for the wavy behavior, and not the vertical main flow. Indeed, at the top half-part of the hot plate, the waviness of the Nusselt number contours becomes reversed (see green dashed lines in Fig. 6g). In this region, where the secondary flows have dissipated, the expected relationship between vertical flow velocity and Nusselt number becomes apparent, i.e. that a higher vertical velocity leads to better heat transfer. All these local effects also results in a modification of the mean shear stress along the isothermal walls $\langle \tau_{zx}(A_y) \rangle$ (see Tab. II and Fig. 10b). As the averaged Nusselt number depicted in Tab. I, the mean shear stress tends to the value obtained in 2D configuration, i.e. 34.55.

To sum up this part, we show that an increase of the horizontal aspect ratio A_y controls the

number and the size of vortices, and that these vortices significantly influence local heat transfer.

TABLE II: Values of the mean shear stress $\langle \tau_{zx}(A_y) \rangle$ at the isothermal wall according to the horizontal aspect ratio A_y. The last column reports its value in the 2D configuration.

A_y	0.13	0.2	0.3	0.4	0.6	0.8	1	2	3	4	2D
$\langle \tau_{zx}(A_y) \rangle$	25.09	28.44	30.41	31.17	32.02	32.45	32.8	33.70	33.98	34.24	34.55

IV. PHYSICAL EXPLANATION OF THE FLOW DYNAMICS

In this section, the discussion focuses on the origin and development of the three-dimensional structures observed in the vertical boundary layers in the form of pairs of counter-rotating longitudinal vortices and the two edge vortices (see previous sections, e.g. Figs. 8a-8d). The main mechanism is the centrifugal effect induced by the main cavity flow.

A. Discussion about central vortices: a Görtler approach

Pairs of counter-rotating longitudinal vortices like those shown in Figs. 8a-8d and 9a-9g can be observed in flows where centrifugal forces play an important role like in wall jets on a concave surface[40], in lid-driven cavity[41], open cavity[42] and close cavity flows[30]. The centrifugal instability occurs when the magnitude of the angular velocity decreases with increasing distance to a center of rotation in regions of the flow where streamlines are closer[43]. In Figures 10a and 10b, twenty five streamlines close to the cold wall are drawn from the emission line $(x = 0.21; 0.25 \leq y \leq 0.5; z = 0.985)$ with a constant spatial step Δy. The z-velocity distribution, which is relevant for centrifugal instability, is not uniform along the cold wall in the y-direction. In the top part of the cavity, the horizontal flow in direction $x > 0$ impacts the cold boundary layer, so that streamlines are curved with a concave curvature; then they are slightly deflected due to a positive or negative y-velocity component.

Thus, it appears that three-dimensional structures triggered by a centrifugal instability inducing counter-rotating vortices exist and may destabilize the boundary layers along the isothermal walls (for $2 \leq A_y \leq 4$). The ratio of the destabilizing inertial and centrifugal forces to the stabilizing

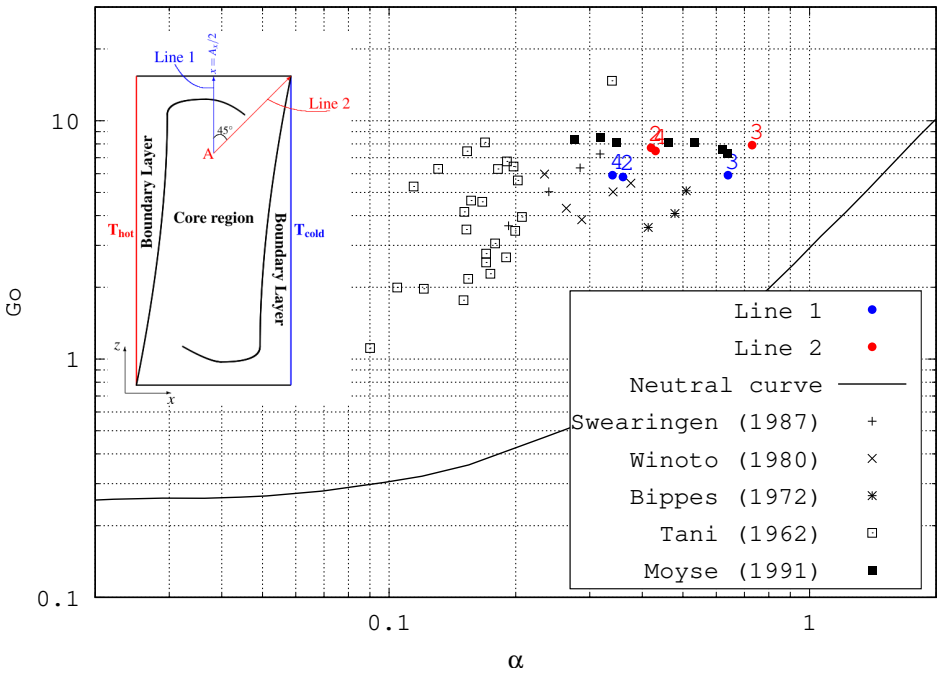

FIG. 11: For three horizontal aspect ratio, $A_y = 2$, 3 and 4, Görtler number versus the dimensionless wavenumber, $\alpha = k\delta_2$. For comparison, the linearized neutral stability curve established by Floryan[44] and various experimental results[45–48] are also plotted. Insert: Flow visualization in a vertical plan $y = 0$ and the lines where Görtler numbers are estimated.

viscous force is expressed in terms of the Görtler number, i.e. a combination of the Reynolds number and a curvature parameter[40,49]:

$$Go = Re_{\delta_2}\sqrt{\frac{\delta_2}{R_c}} = \frac{U_\infty \delta_2}{\nu}\sqrt{\frac{\delta_2}{R_c}} \tag{9}$$

where U_∞ is the maximum horizontal velocity at $x = 0.125$, δ_2 is the boundary layer momentum-loss thickness, ν is the kinematic viscosity and R_c is the radius of curvature of a streamline for which the center of the circle is chosen to be a stagnation point on the line $x = \frac{A_x}{2}$ (see point A in the insert in Fig. 11). In Fig. 11, values of Görtler number are plotted versus the dimensionless wavenumbers ($\alpha = k\delta_2 = \frac{2\pi\delta_2}{\lambda}$) for three horizontal aspect ratios, $A_y = 2$, 3 and 4, along the red and blue lines (see the insert in Fig. 11). The values of λ are determined using Figs. 9e, 9f and

9g. A comparison with experimental results and the linearized neutral stability curve established by Floryan[44] about boundary layers over concave walls are also plotted in Fig. 11. It can be observed that the six points are well positioned above the theoretical neutral curve, that is to say in the unstable region, and close to the experimental results obtained in the case of laminar boundary layers on concave surfaces[45–48]. This analysis suggests that the pairs of counter-rotating longitudinal vortices developped in DHC with horizontal aspect ratio, $A_y = 2$, 3 and 4 are generated via a Görtler instability mechanism. Of course, the counter-rotating longitudinal (and horizontal) vortices calculated at $x = 0.125$ are generated by the curvature of the flow from the hot wall (upper left part of DHC; see the insert in Fig. 11). The values of the Görtler number only increase as a function of the position in the streamwise direction as long as the flow approaches the corner, and not afterwards (the calculated values along the red line are greater than those along the blue line). Görtler values remain independent of A_y (for $A_y > 1$) while the dimensionless wavenumber, α, depends on the streamwise positions.

B. Discussion about central vortices: a Taylor-Couette approach

To explain the central vortices, an analogy can also be done with Taylor-Couette flow[50]. Indeed, we can consider an inner region as a rotating cylinder of axis y and centre ($x = \frac{W}{2}$, $z = \frac{H}{2}$). The radius of the inner cylinder is determined from the maximum velocity induced by natural convection in the boundary layer u_{ref}. In this analogy this region can be considered as a rotating solid body. The velocity decreases radially between (the inner radius) and the cavity wall (the outer radius). In this way, considering the confined flow between two cylinders is a rough approximation of the recirculation inside the DHC. In our case, the outer cylinder is at the rest and the Taylor-Couette cells depend on the Reynolds number which is based on the angular velocity of the inner cylinder and the gap width[51]:

$$\mathrm{Re}_t = \frac{u_{ref}(R_o - R_i)}{\nu} \tag{10}$$

where $u_{ref} \approx 0.25$ and $R_o = 0.125$ and $R_i \approx 0.115$ are the radii of the outer and inner cylinder, respectively. For the small gap limit, *i.e.* $(R_o - R_i) \ll R_i$, the critical Reynolds number is given by[51]:

$$\mathrm{Re}_{t_{cr}} = 41.18\sqrt{\frac{R_i}{R_o - R_i}} \tag{11}$$

Using these formulae, we find a maximum Reynolds number, $\mathrm{Re}_t \approx 39$, while the critical Reynolds number is $\mathrm{Re}_{t_{cr}} = 133$. These values demonstrate that the centrifugal instability in the DHC can-

not be identified with the Taylor-Couette instability. Moreover, the Eq. 11 is established from Taylor-Couette analysis where the effects of the endwalls on the flow are not taken into account theoretically by assuming infinitely long cylinder[51]. In the same way, to simulate counter-rotating longitudinal vortices on concave surface (Görtler analysis), periodic boundary conditions in the spanwise direction are often applied[52]. So it could be expected a strong influence of boundary conditions on the pairs of counter-rotating longitudinal vortices.

C. Discussion on edge vortices

To explain the two edge vortices, an analogy can be done with the Ekman vortices which are observed in Taylor-Couette configurations even if the Taylor number is subcritical[50,53]. In Fig. 12a isosurfaces of the helicity $w.\omega_z$ per unit of volume of the flow are plotted for visualizing these edge vortices. The level of helicity appears to be higher in the two edge vortices than for the pairs of counter-rotating longitudinal vortices positioned in the middle boundary layer (Görtler vortices). For these isosurfaces, it can be observed again that the edge vortices are more energetic than Görtler vortices. Moreover, these Görtler vortices show a helicity which decreases as y tends to $\frac{A_y}{2}$. This high helicity is due to a greater heated surface of a parcel of fluid along the edge (sum of the constant temperature and the temperature derived from an adiabatic condition) coupled to the friction along the adiabiatic walls. Thus, these two vortices that remain along the edge, joining the back or front wall to the hot or cold wall, seems to be Ekman like vortices[53,54] (or Eckhaus like vortices). In order to show the role of boundary conditions on two vortices along the edge, simulations are performed with slip boundary conditions on rear and front adiabatic walls, and the helicity is also calculated. The absence of edge vortices can be observed in Fig. 12b. So the no-slip boundary conditions play an essential role on the generation of edge vortices.

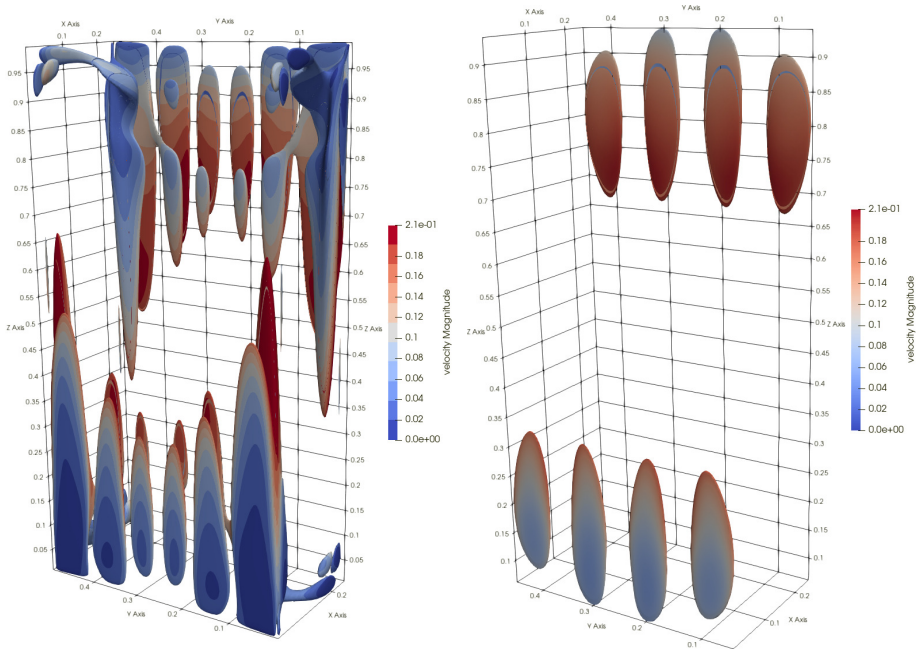

(a) no-slip boundary conditions

(b) slip boundary conditions.

FIG. 12: For $Ra = 10^8$ and $A_y = 2$, isosurfaces of the helicity $w.\omega_z = \pm 0.3, \pm 0.2 \pm 0.15 \pm 0.1 \pm 0.05$ are plotted for: a) no-slip conditions on rear and front walls; b) slip conditions on rear and front walls. The magnitude of velocity is superimposed.

V. CONCLUSION

In the present work 3D direct numerical simulations were conducted to study the effect of the depth of an air-filled differentially heated cavity of vertical aspect ratio, A_z, equals to four, by means of the spectral element method programmed in the code Nek5000. This paper focuses on a laminar flow in such a DHC (without radiative effect) at a Rayleigh number $Ra = 10^8$, just below the first bifurcation, but greater than 2.141×10^7 to ensure that a flow in the $y-$direction is observed. However, it is noted that all flows are always steady even if the horizontal aspect ratio A_y increases. This study shows first the impact of the rear and front boundary conditions on the topology of the flow. Second the influence of horizontal aspect ratio is studied in details. This

aspect ratio controls the structure number: when $A_y \leq 1$, only edge vortices are observed; when $A_y > 1$, between the edge vortices some central structures appear whose number increases with A_y. The structures which are not edge vortices seem generated by a Görtler instability at the bottom of the hot plate and at the top of the cold plate. They have not enough energy to have a constant pattern along the isothermal walls. However, they strongly modify the local heat transfer at the isothermal walls. The edge vortices seem to be Ekman-like vortices, and their existence seems to increase the strength of the Görtler vortices. Despite those 3D structures, the global heat transfer and the global flow dynamics are characterized by magnitudes whose values tend to approach those of a 2D configuration as the depth of the cavity increases. Finally, since the structures are now well-known just before the first transition, it would be interesting to study the influence of the Görtler vortices on the cavity flow and heat transfer when the Rayleigh number is increased.

ACKNOWLEDGMENTS

The authors would like to thank the financial support provided by ANID (Fondecyt project 1171281). The authors also thank Yuri Ivanov for technical support of the CCTVAL (USM HPC cluster) where a part of the evaluations were carried out. N. T. thanks UTFSM through its Programa de Incentivos a la investigación científica (PIIC) on its 2017 version.

Accepted to Phys. Fluids 10.1063/5.0100218

REFERENCES

[1]G. de Vahl Davis, "Laminar natural convection in an enclosed rectangular cavity," International Journal of Heat and Mass Transfer **11**, 1675–1693 (1968).

[2]D. Saury, N. Rouger, F. Djanna, and F. Penot, "Natural convection in an air-filled cavity: Experimental results at large rayleigh numbers," International Communications in Heat and Mass Transfer **38**, 679–687 (2011).

[3]P. Belleoud, D. Saury, and D. Lemonnier, "Coupled velocity and temperature measurements in an air-filled differentially heated cavity at $\mathrm{Ra} = 1.2 \times 10^{11}$," International Journal of Thermal Sciences **123**, 151–161 (2018).

[4]V. Kishor, S. Singh, and A. Srivastava, "Flow instabilities and heat transfer in a differentially heated cavity placed at varying inclination angles: Non-intrusive measurements," Physics of Fluids **33**, 094103 (2021).

[5]X. Wen, L.-P. Wang, and Z. Guo, "Development of unsteady natural convection in a square cavity under large temperature difference," Physics of Fluids **33**, 084108 (2021).

[6]U. Prasopchingchana, "Direct numerical simulation of natural convection in a square cavity at high rayleigh numbers via the lagrange interpolating polynomial scheme," International Journal of Thermal Sciences **172**, 107276 (2022).

[7]G. D. V. Davis and I. P. Jones, "Natural convection in a square cavity: A comparison exercise," International Journal for Numerical Methods in Fluids **3**, 227–248 (1983).

[8]S. Xin and P. Le Quéré, "An extended chebyshev pseudo-spectral benchmark for the 8:1 differentially heated cavity," International Journal for Numerical Methods in Fluids **40**, 981–998 (2002).

[9]J. Patterson and J. Imberger, "Unsteady natural convection in a rectangular cavity," Journal of Fluid Mechanics **100**, 65 (1980).

[10]R. J. A. Janssen and R. A. W. M. Henkes, "Influence of prandtl number on instability mechanisms and transition in a differentially heated square cavity," Journal of Fluid Mechanics **290**, 319–344 (1995).

[11]S. Xin and P. Le Quéré, "Direct numerical simulations of two-dimensional chaotic natural convection in a differentially heated cavity of aspect ratio 4," Journal of Fluid Mechanics **304**, 87–118 (1995).

[12]P. L. Quéré and M. Behnia, "From onset of unsteadiness to chaos in a differentially heated square cavity," Journal of Fluid Mechanics **359**, 81–107 (1998).

[13]S. Xin and P. Le Quéré, "Stability of two-dimensional (2d) natural convection flows in air-filled differentially heated cavities: 2d/3d disturbances," Fluid Dynamics Research **44**, 031419 (2012).

[14]L. Oteski, Y. Duguet, L. Pastur, and P. L. Quéré, "Quasiperiodic routes to chaos in confined two-dimensional differential convection," Physical Review E **92**, 043020 (2015).

[15]O. Turan, N. Chakraborty, and R. J. Poole, "Laminar natural convection of bingham fluids in a square enclosure with differentially heated side walls," Journal of Non-Newtonian Fluid Mechanics **165**, 901–913 (2010).

[16]Y. Liu, Y. Bian, Y. Zhao, S. Zhang, and Q. Suo, "Scaling laws for the transient convective flow in a differentially and linearly heated rectangular cavity at pr > 1," Physics of Fluids **31**, 043601 (2019), https://doi.org/10.1063/1.5087907.

[17]S. Xin and P. Le Quéré, "Linear stability analyses of natural convection flows in a differentially heated square cavity with conducting horizontal walls," Physics of Fluids **13**, 2529–2542 (2001).

[18]F. Trias, A. Gorobets, M. Soria, and A. Oliva, "Direct numerical simulation of a differentially heated cavity of aspect ratio 4 with rayleigh numbers up to $\mathrm{Ra} = 10^{11}$, part i: Numerical methods and time-averaged flow," International Journal of Heat and Mass Transfer **53**, 665–673 (2010).

[19]D. Kizildag, F. Trias, I. Rodríguez, and A. Oliva, "Large eddy and direct numerical simulations of a turbulent water-filled differentially heated cavity of aspect ratio 5," International Journal of Heat and Mass Transfer **77**, 1084–1094 (2014).

[20]G. Colomer, M. Costa, R. Cònsul, and A. Oliva, "Three-dimensional numerical simulation of convection and radiation in a differentially heated cavity using the discrete ordinates method," International Journal of Heat and Mass Transfer **47**, 257–269 (2004).

[21]S. Xin, J. Salat, P. Joubert, A. Sergent, F. Penot, and P. L. Quéré, "Resolving the stratification discrepancy of turbulent natural convection in differentially heated air-filled cavities. part III: A full convection–conduction–surface radiation coupling," International Journal of Heat and Fluid Flow **42**, 33–48 (2013).

[22]L. Soucasse, P. Rivière, A. Soufiani, S. Xin, and P. L. Quéré, "Transitional regimes of natural convection in a differentially heated cubical cavity under the effects of wall and molecular gas radiation," Physics of Fluids **26**, 024105 (2014).

[23]Y. Billaud, D. Saury, and D. Lemonnier, "Numerical investigation of coupled natural convection and radiation in a differentially heated cubic cavity filled with humid air. effects of the cavity

size," Numerical Heat Transfer, Part A: Applications **72**, 495–518 (2017).

[24]A. Sergent, S. Xin, P. Joubert, P. L. Quéré, J. Salat, and F. Penot, "Resolving the stratification discrepancy of turbulent natural convection in differentially heated air-filled cavities – part i: Reference solutions using chebyshev spectral methods," International Journal of Heat and Fluid Flow **39**, 1–14 (2013).

[25]P. L. Quéré, "Accurate solutions to the square thermally driven cavity at high rayleigh number," Computers & Fluids **20**, 29–41 (1991).

[26]P. L. Quéré and T. A. de Roquefort, "Transition to unsteady natural convection of air in vertical differentially heated cavities: influence of thermal boundary conditions on the horizontal walls," in *Proceeding of International Heat Transfer Conference 8* (Begellhouse, 1986).

[27]E. Nobile, "Simulation of time-dependent ow in cavities with the additive-correction multigrid method, part ii: applications," Numerical Heat Transfer, Part B: Fundamentals **30**, 351–370 (1996).

[28]F. X. Trias, M. Soria, A. Oliva, and C. D. Pérez-Segarra, "Direct numerical simulations of two- and three-dimensional turbulent natural convection flows in a differentially heated cavity of aspect ratio 4," Journal of Fluid Mechanics **586**, 259–293 (2007).

[29]S. Paolucci, "The differentially heated cavity," Sadhana **19**, 619–647 (1994).

[30]R. J. A. Janssen and R. A. W. M. Henkes, "Instabilities in three-dimensional differentially-heated cavities with adiabatic horizontal walls," Physics of Fluids **8**, 62–74 (1996).

[31]J. Salat, S. Xin, P. Joubert, A. Sergent, F. Penot, and P. L. Quéré, "Experimental and numerical investigation of turbulent natural convection in a large air-filled cavity," International Journal of Heat and Fluid Flow **25**, 824–832 (2004).

[32]P. Fischer, J. Lottes, and S. Kerkemeier, "Nek5000: open source spectral element cfd solver," (2016).

[33]A. T. Patera, "A spectral element method for fluid dynamics: Laminar flow in a channel expansion," Journal of Computational Physics **54**, 468–488 (1984).

[34]M. O. Deville, P. F. Fischer, and E. H. Mund, *High-Order Methods for Incompressible Fluid Flow* (Cambridge University Press, 2002).

[35]O. Skurtys, *Contribution au contrôle de la convection naturelle par excitation thermique des couches limites en cavité différentiellement chauffée*, Thèse (2004), université de Poitiers.

[36]F. Penot, O. Skurtys, and D. Saury, "Preliminary experiments on the control of natural convection in differentially-heated cavities," International Journal of Thermal Sciences **49**, 1911–1919

(2010).

[37]J. Jeong and F. Hussain, "On the identification of a vortex," Journal of Fluid Mechanics **285**, 69–94 (1995).

[38]V. Kishor, S. Singh, and A. Srivastava, "On the identification of flow instabilities in a differentially-heated closed cavity: Non-intrusive measurements," International Journal of Heat and Mass Transfer **147**, 118933 (2020).

[39]N. Thiers, R. Gers, and O. Skurtys, "Heat transfer enhancement by localised time varying thermal perturbations at hot and cold walls in a rectangular differentially heated cavity," International Journal of Thermal Sciences **151**, 106245 (2020).

[40]W. S. Saric, "Görtler vortices," Annual Reviews **26**, 379–409 (1994).

[41]S. Albensoeder and H. C. Kuhlmann, "Nonlinear three-dimensional flow in the lid-driven square cavity," Journal of Fluid Mechanics **569**, 465 (2006).

[42]F. Picella, J.-C. Loiseau, F. Lusseyran, J.-C. Robinet, S. Cherubini, and L. Pastur, "Successive bifurcations in a fully three-dimensional open cavity flow," Journal of Fluid Mechanics **844**, 855–877 (2018).

[43]A. Y. Gelfgat, "Linear instability of the lid-driven flow in a cubic cavity," Theoretical and Computational Fluid Dynamics **33**, 59–82 (2019).

[44]J. M. Floryan, "Görtler instability of boundary layers over concave and convex walls," Physics of Fluids **29**, 2380 (1986).

[45]J. D. Swearingen and R. F. Blackwelder, "The growth and breakdown of streamwise vortices in the presence of a wall," Journal of Fluid Mechanics **182**, 255 (1987).

[46]S. Winoto and R. Crane, "Vortex structure in laminar boundary layers on a concave wall," International Journal of Heat and Fluid Flow **2**, 221–231 (1980).

[47]H. Bippes, *Experimentelle Untersuchung des laminar-turbulenten Umschlags an einer parallel angeströmten konkaven Wand* (Springer Berlin Heidelberg).

[48]I. Tani, "Production of longitudinal vortices in the boundary layer along a concave wall," Journal of Geophysical Research **67**, 3075–3080 (1962).

[49]P. G. Drazin, *Introduction to Hydrodynamic Stability* (Cambridge University Press, 2015).

[50]P. Chossat and G. Iooss, *The Couette-Taylor Problem* (Springer New York, 1994).

[51]D. J. Tritton, *Physical Fluid Dynamics* (Springer Netherlands, 1977).

[52]M. Méndez, M. S. Shadloo, and A. Hadjadj, "Heat-transfer analysis of a transitional boundary layer over a concave surface with görtler vortices by means of direct numerical simulations,"

32, 074111 (2020).

[53]O. Czarny, E. Serre, P. Bontoux, and R. M. Lueptow, "Interaction between ekman pumping and the centrifugal instability in taylor–couette flow," Physics of Fluids **15**, 467–477 (2003).

[54]G. Ahlers, D. S. Cannell, M. A. Dominguez-Lerma, and R. Heinrichs, "Wavenumber selection and eckhaus instability in couette-taylor flow," Physica D: Nonlinear Phenomena **23**, 202–219 (1986).

Accepted to Phys. Fluids 10.1063/5.0100218

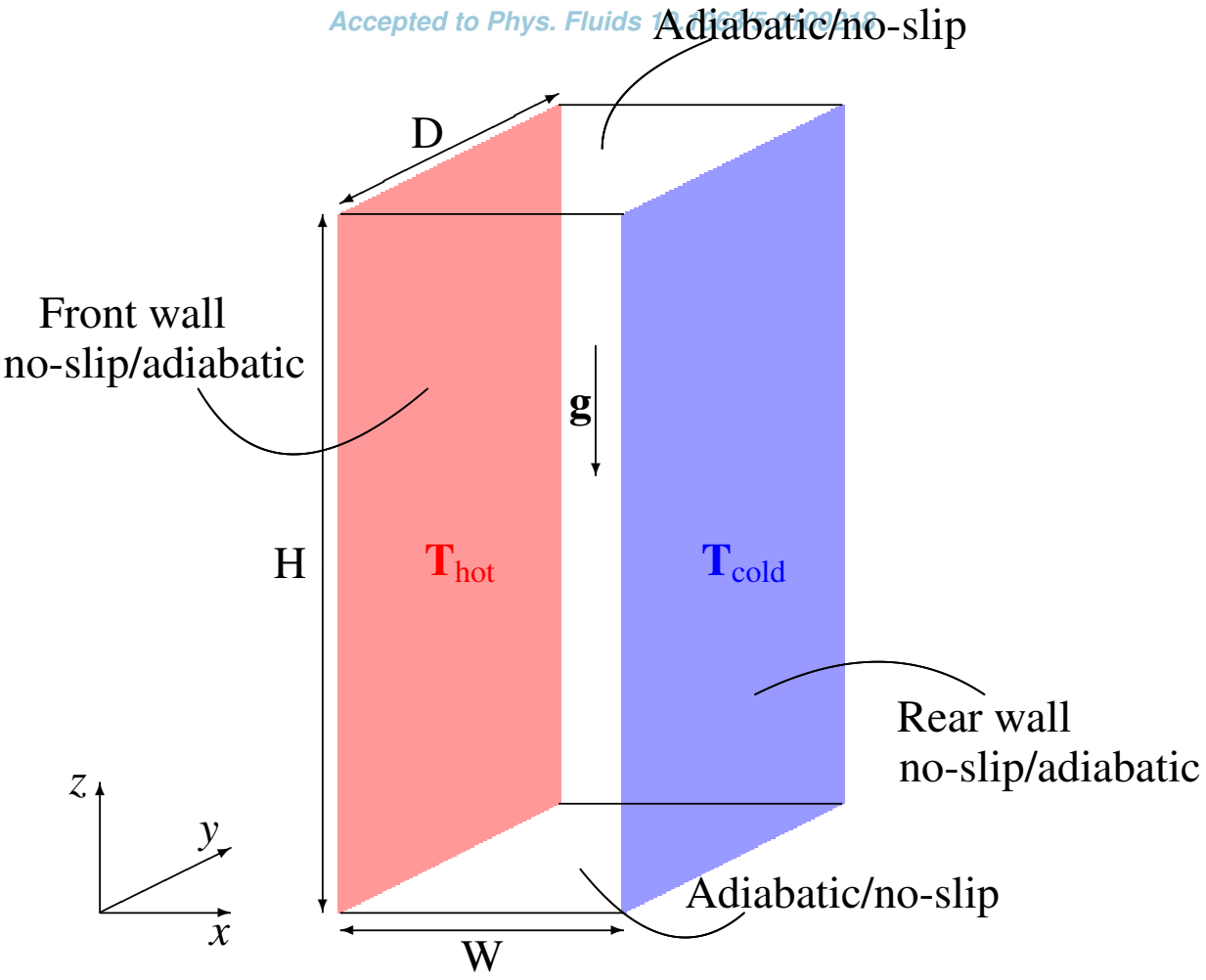

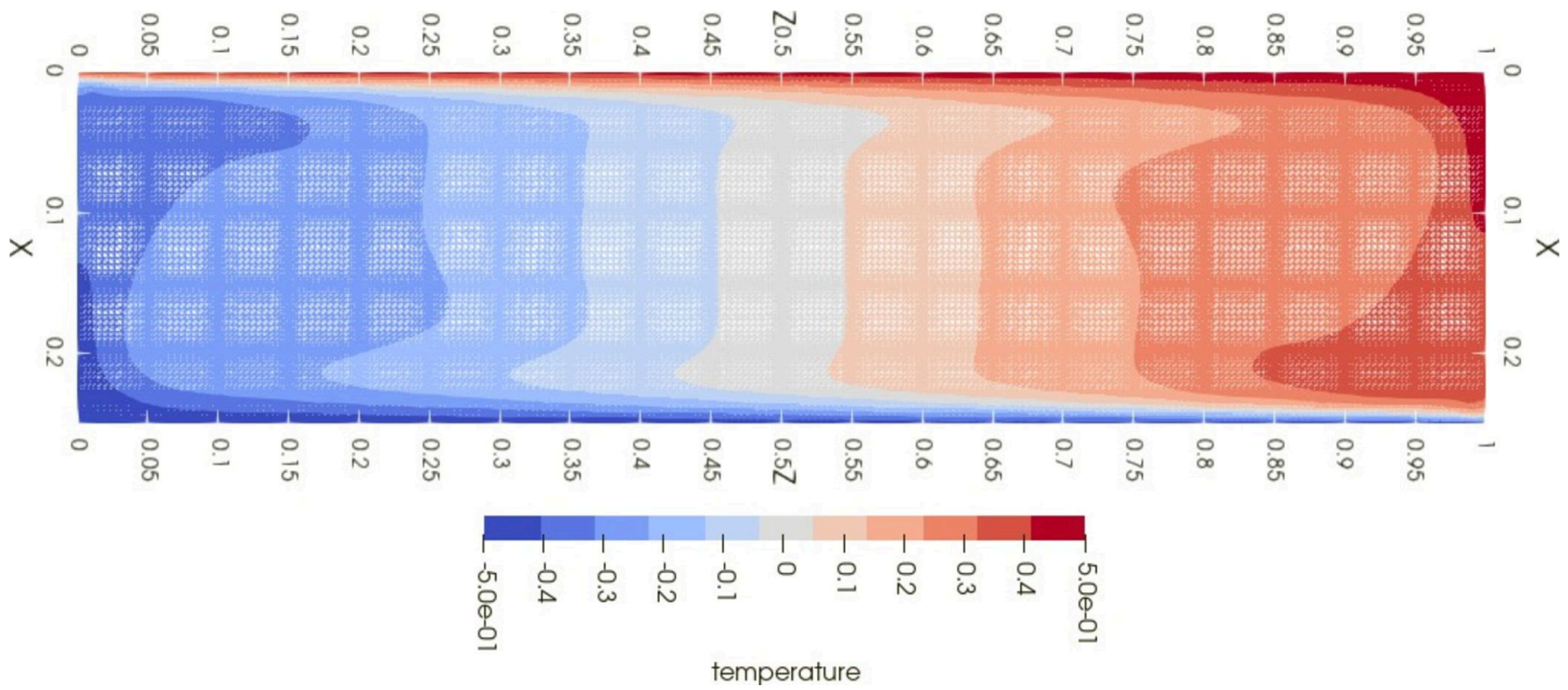

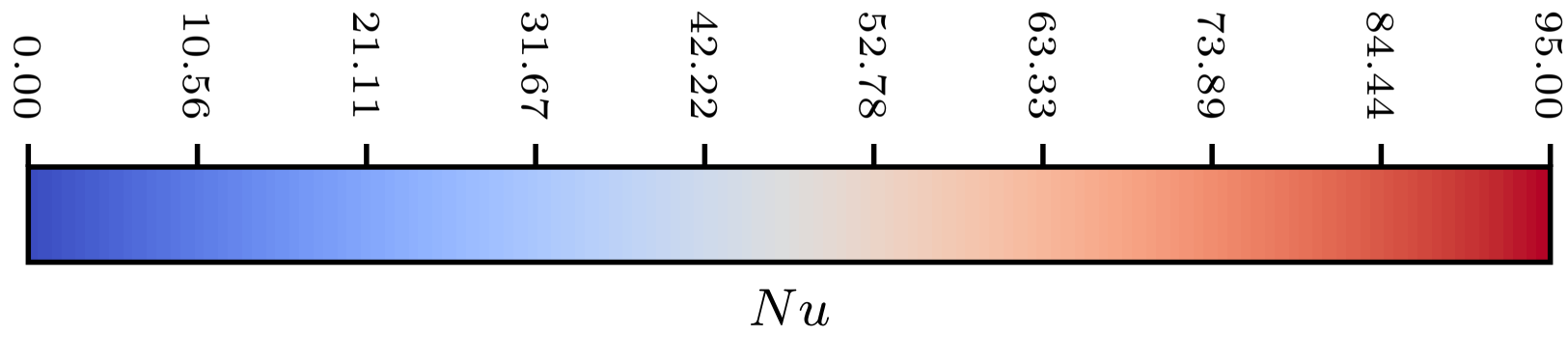

PLEASE CITE THIS ARTICLE AS DOI: 10.1063/5.0100218

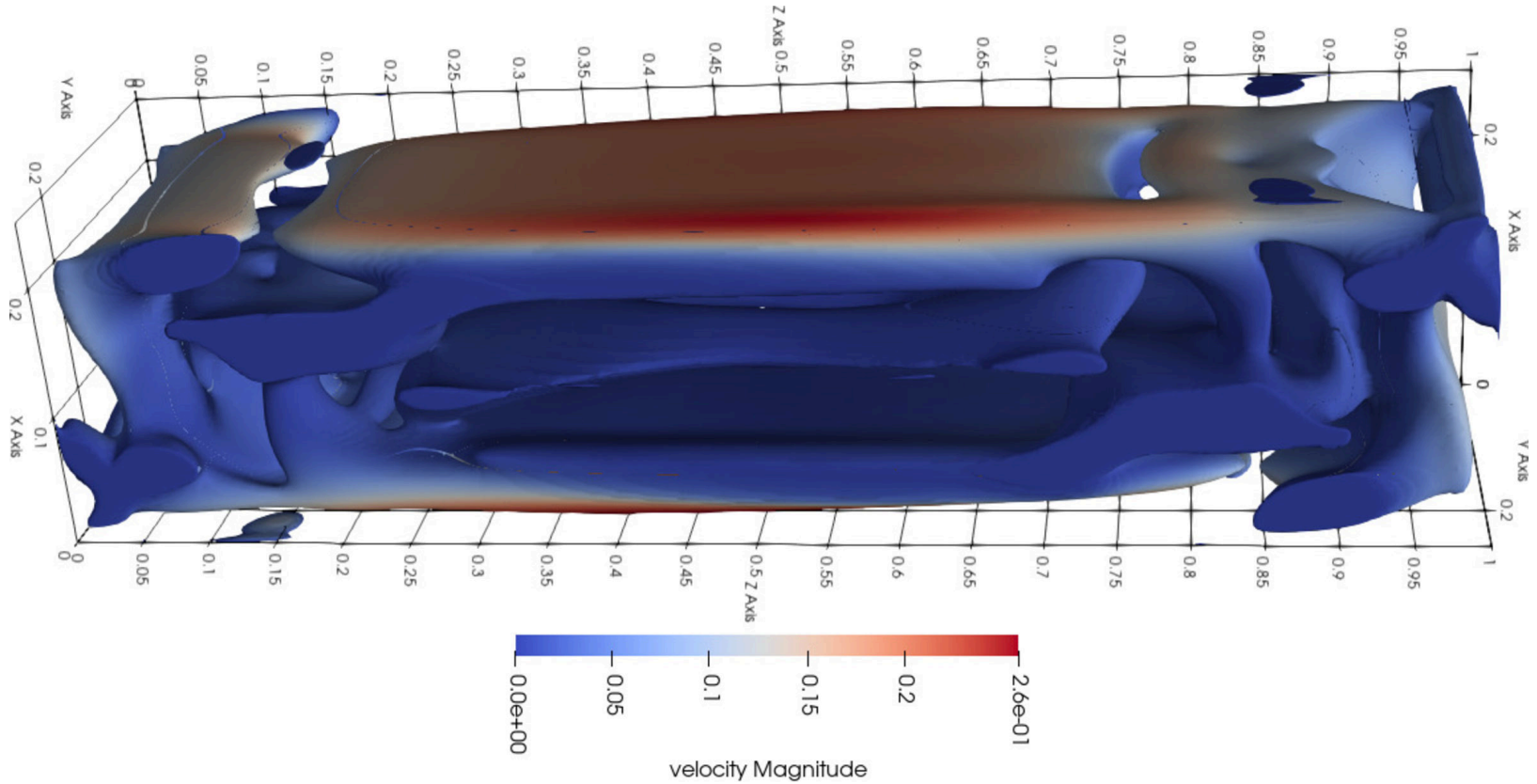

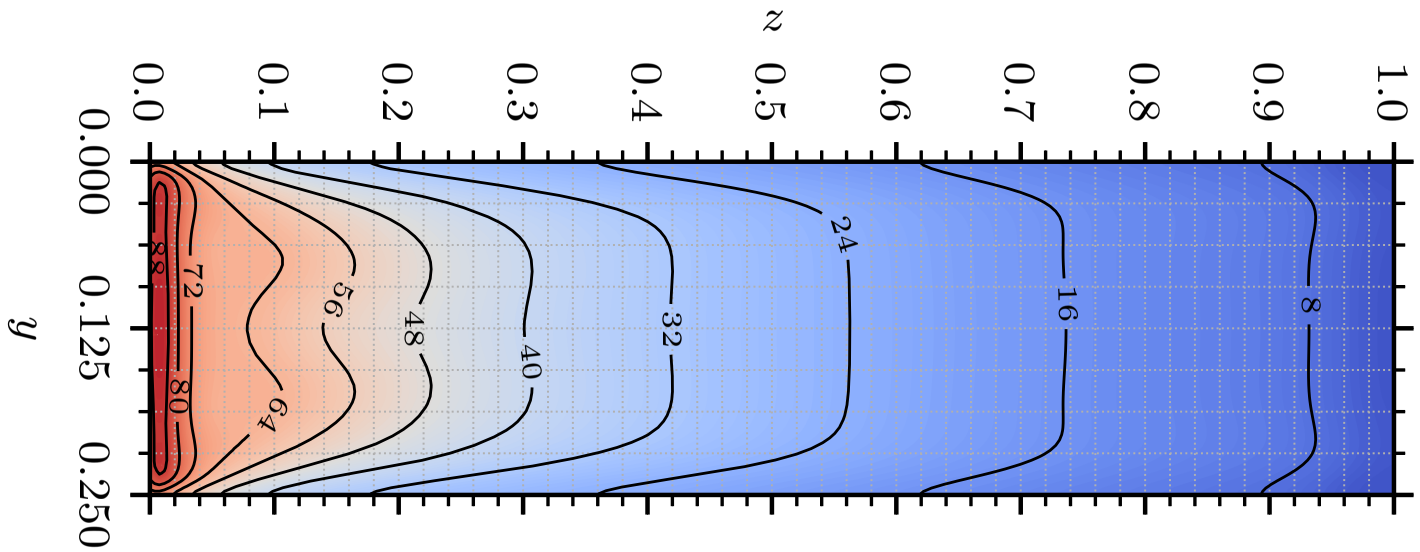

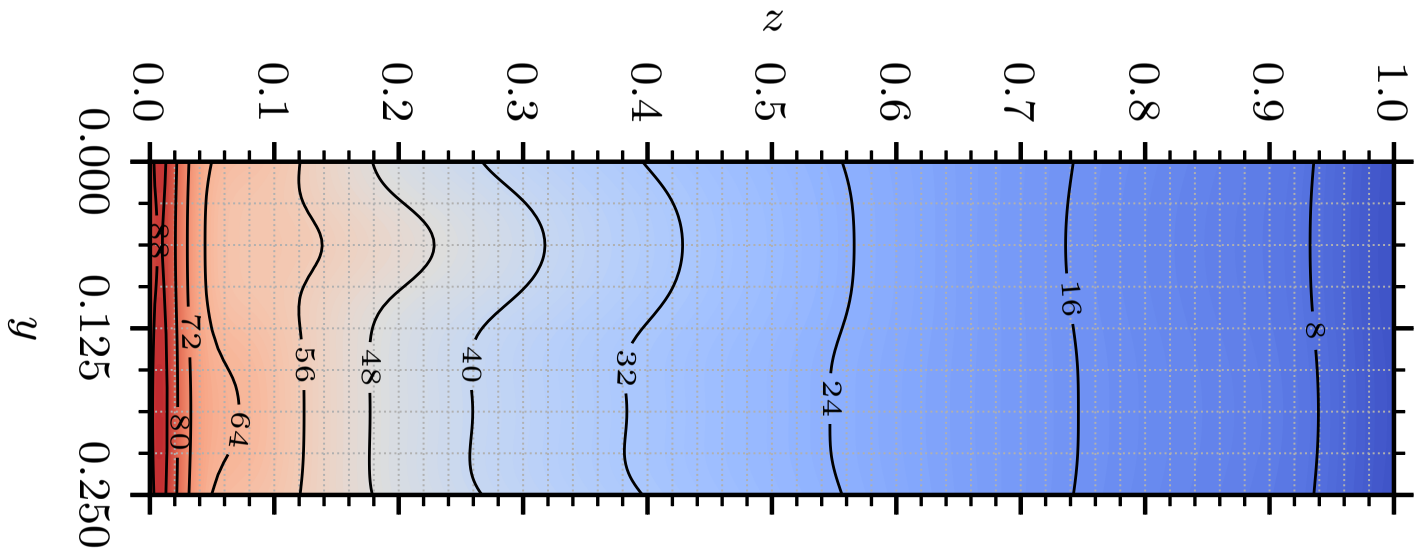

PLEASE CITE THIS ARTICLE AS DOI: 10.1063/5.0100218

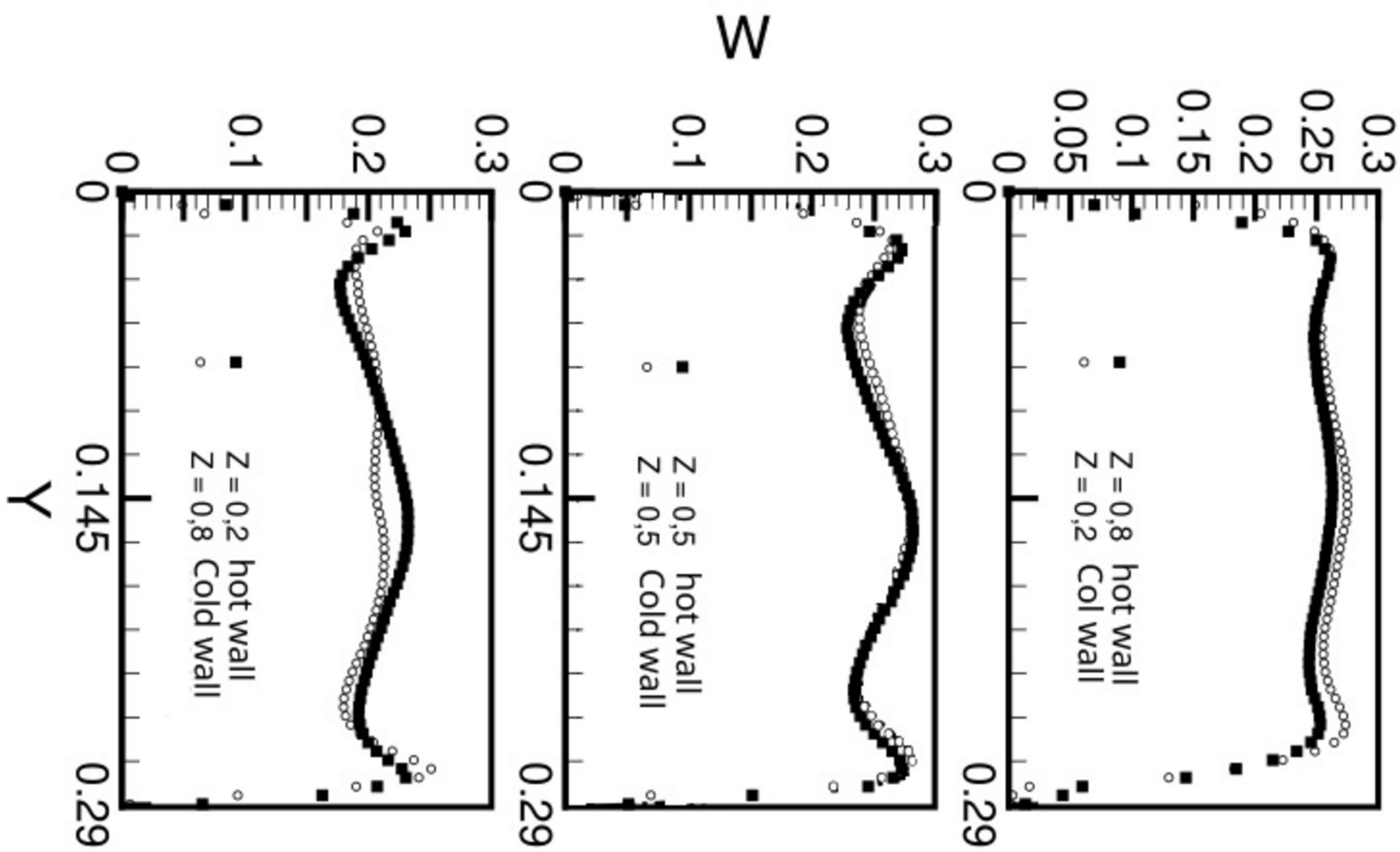

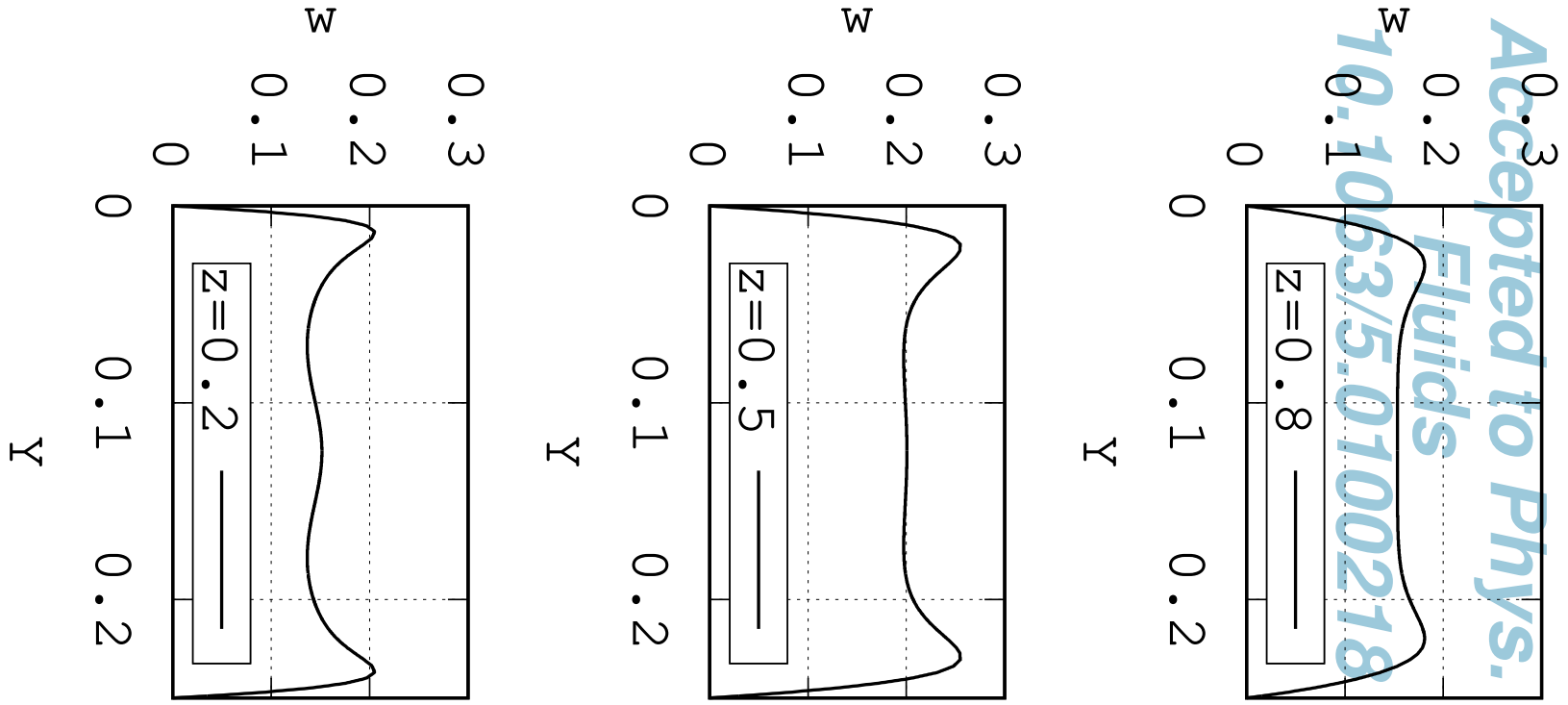

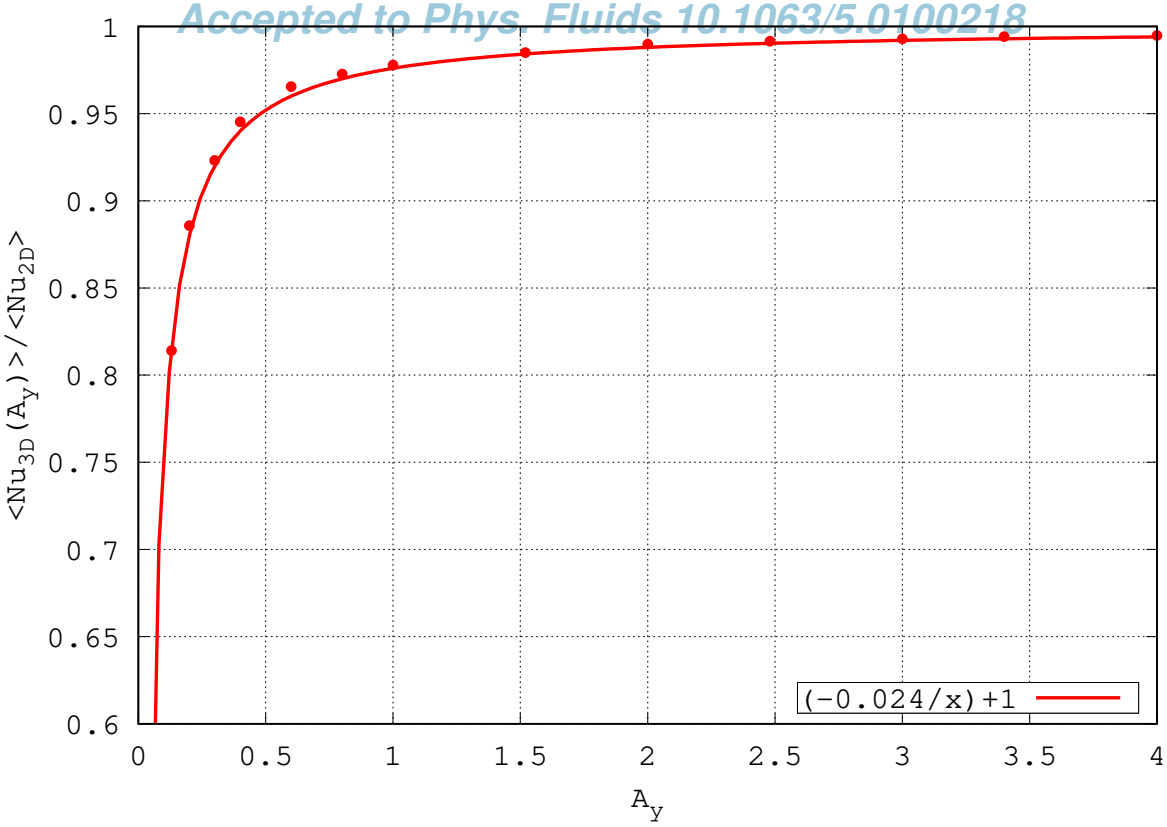

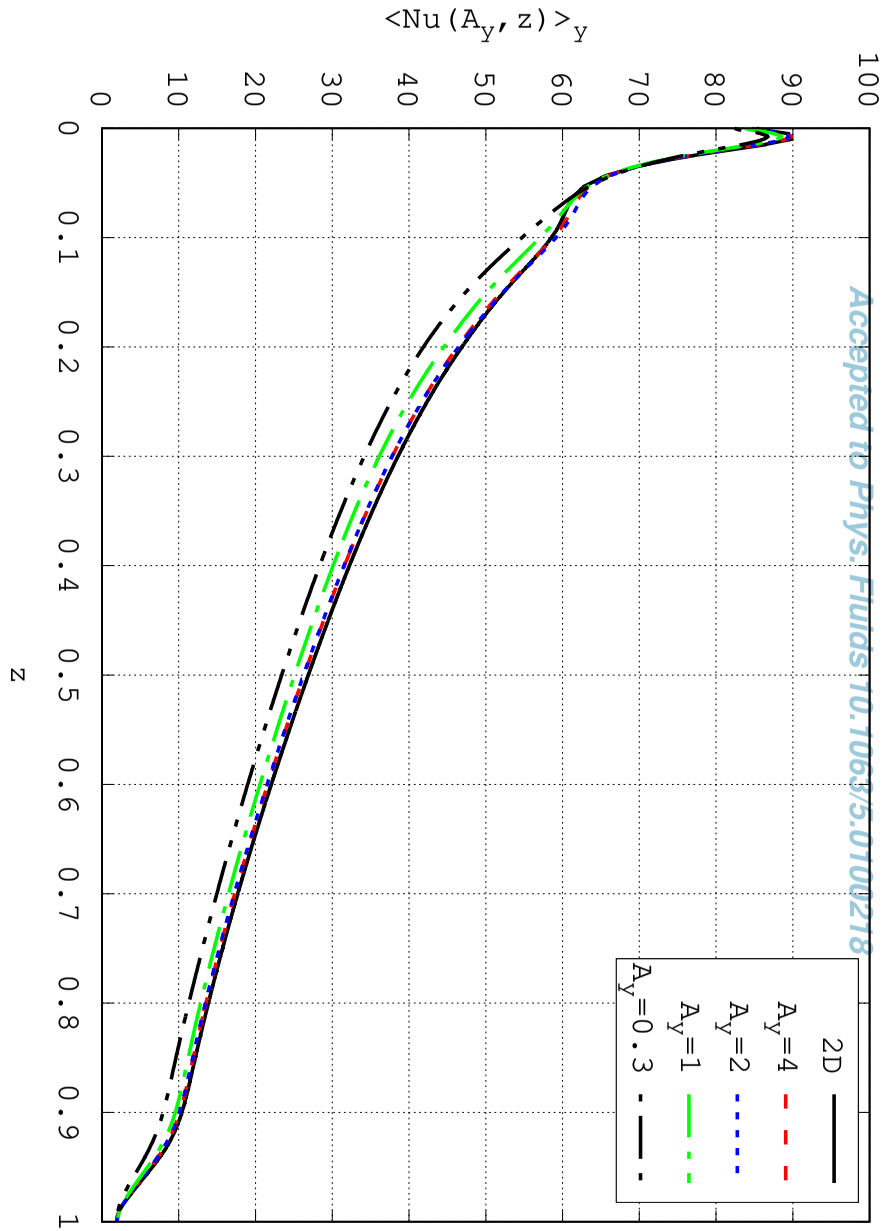

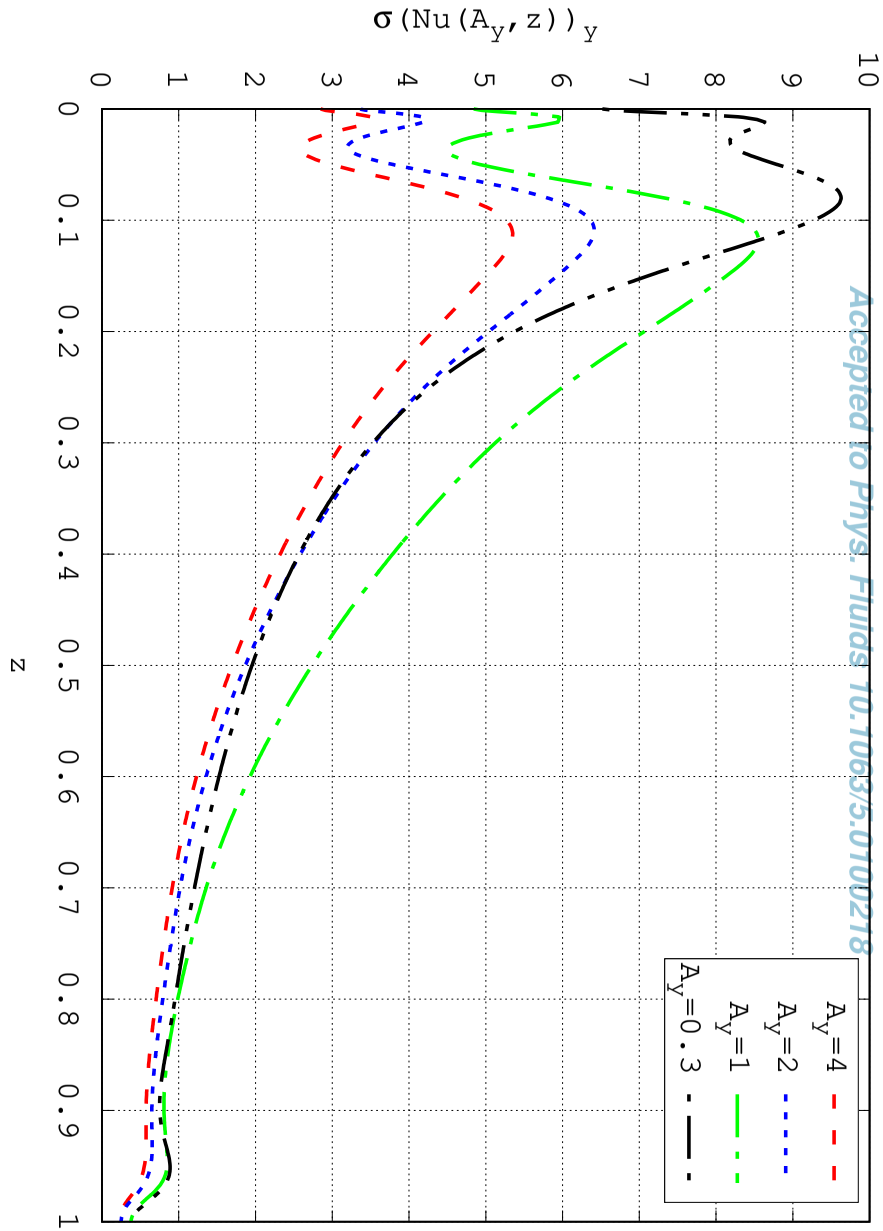

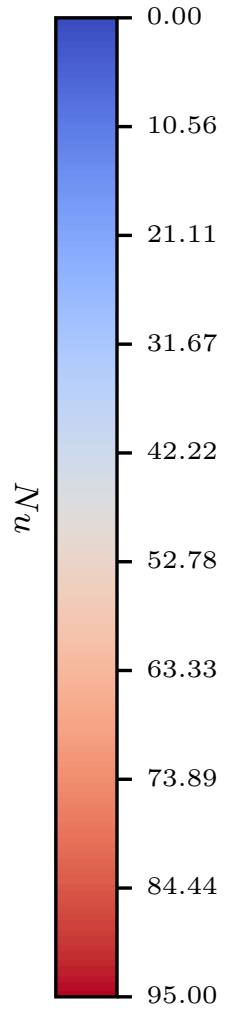

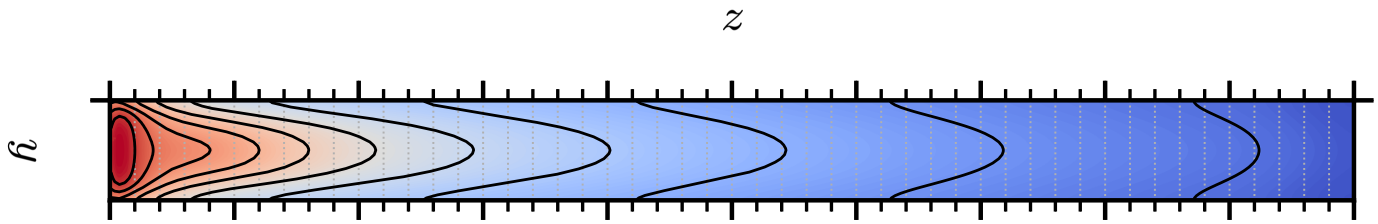

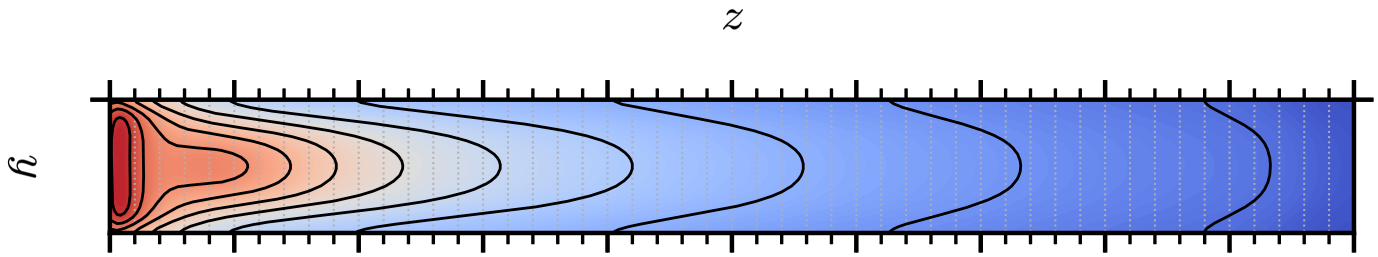

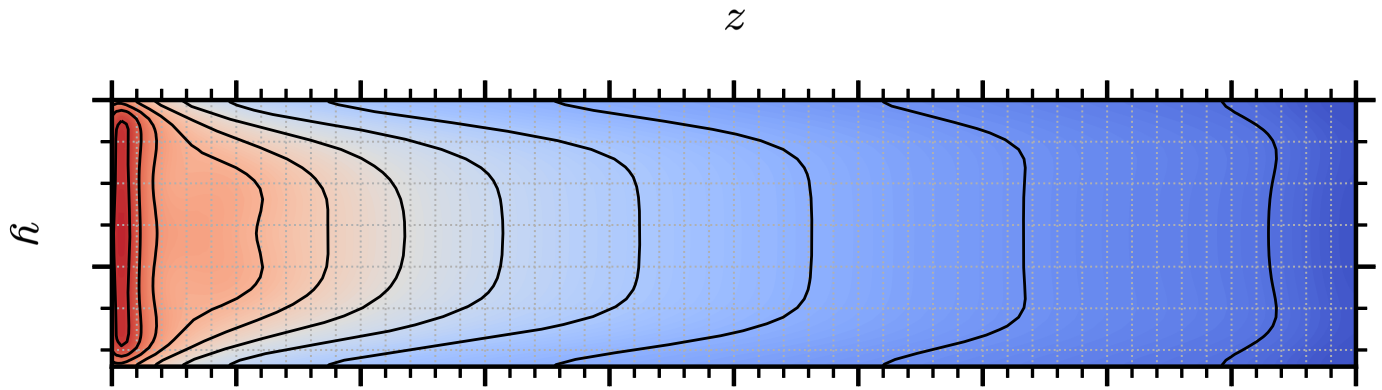

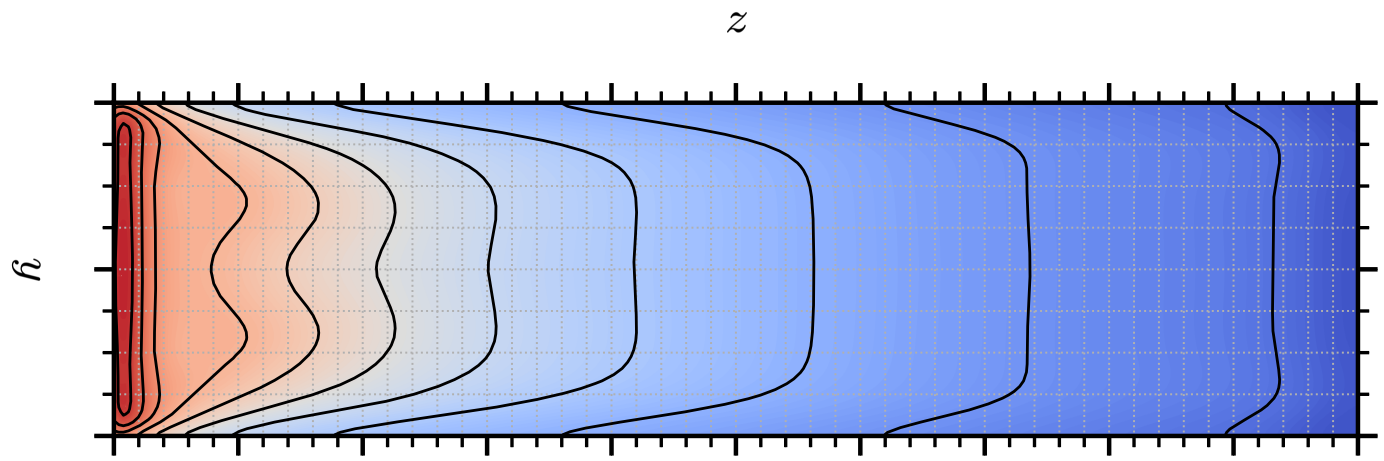

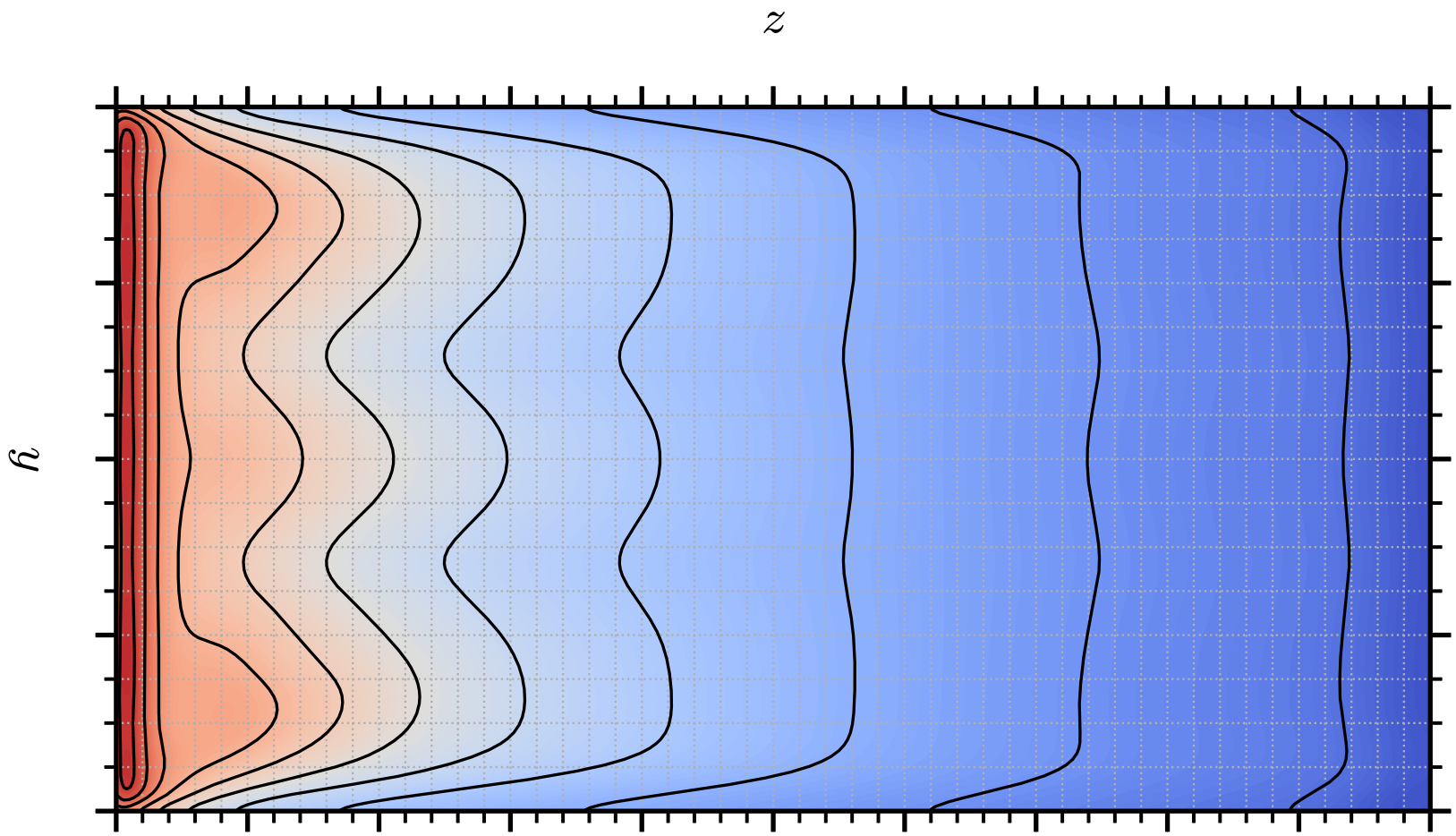

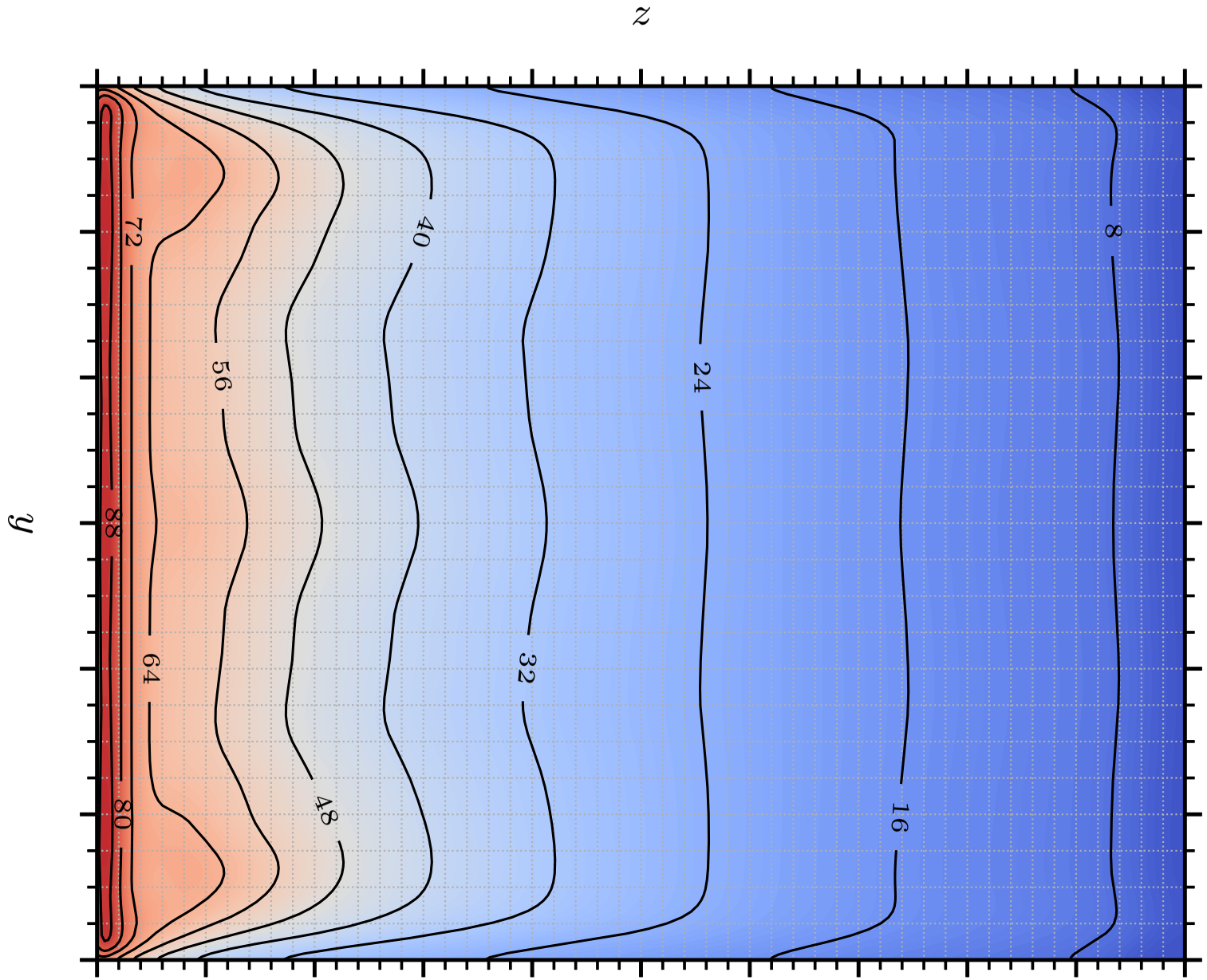

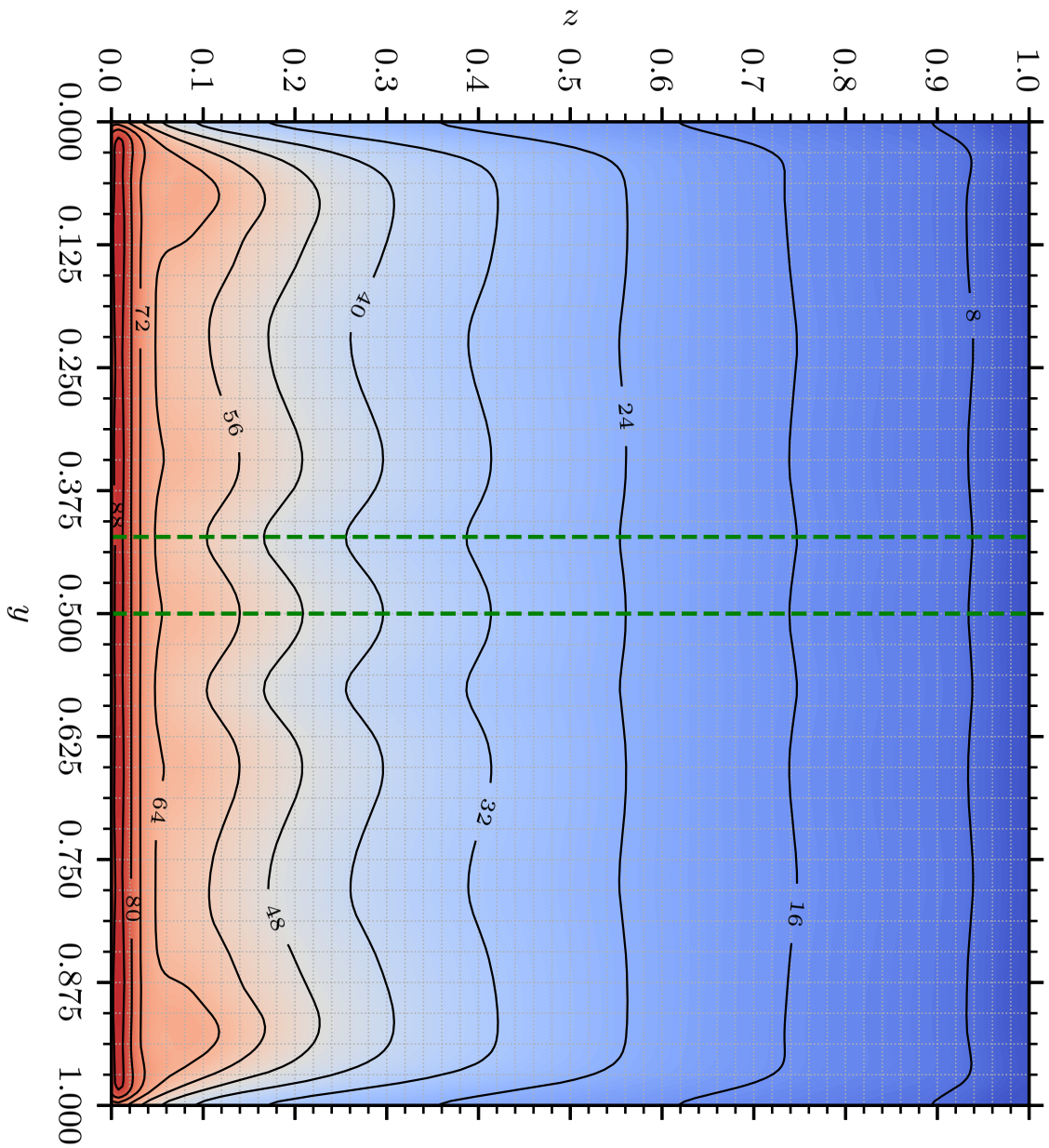

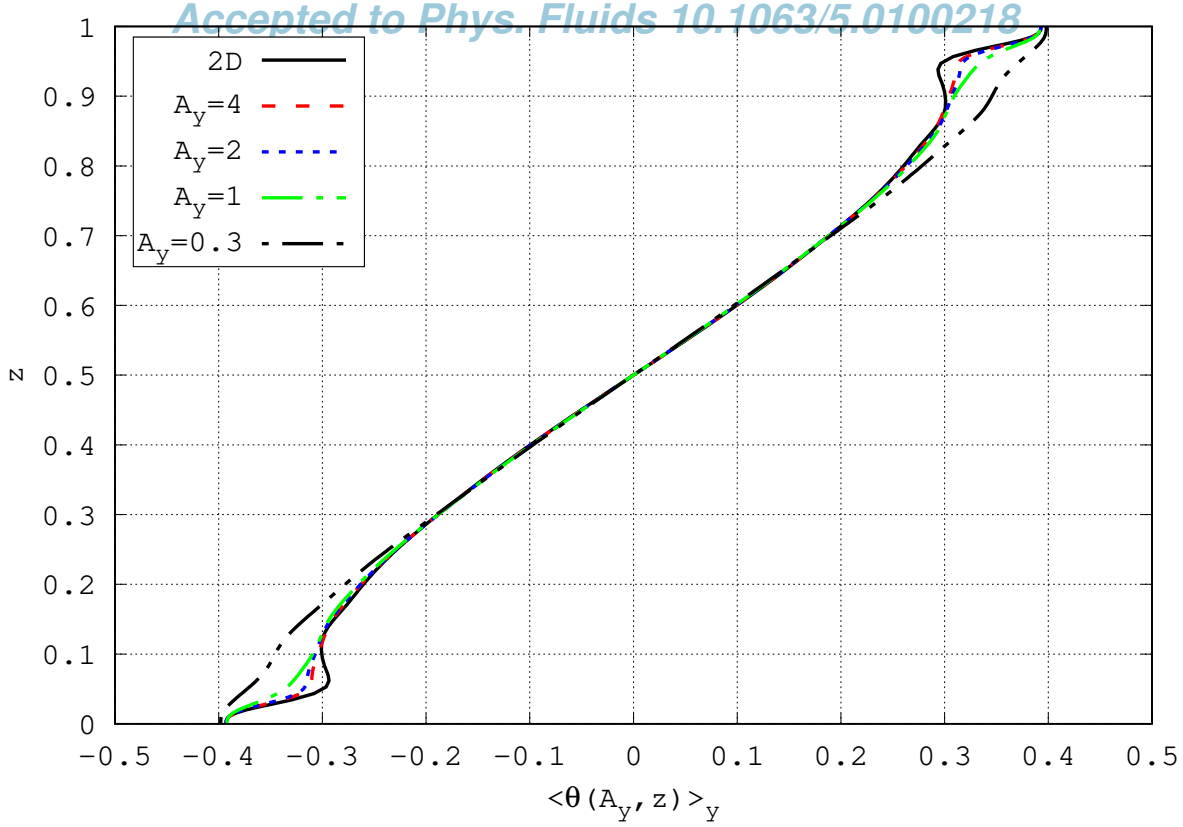

PLEASE CITE THIS ARTICLE AS DOI: 10.1063/5.0100218

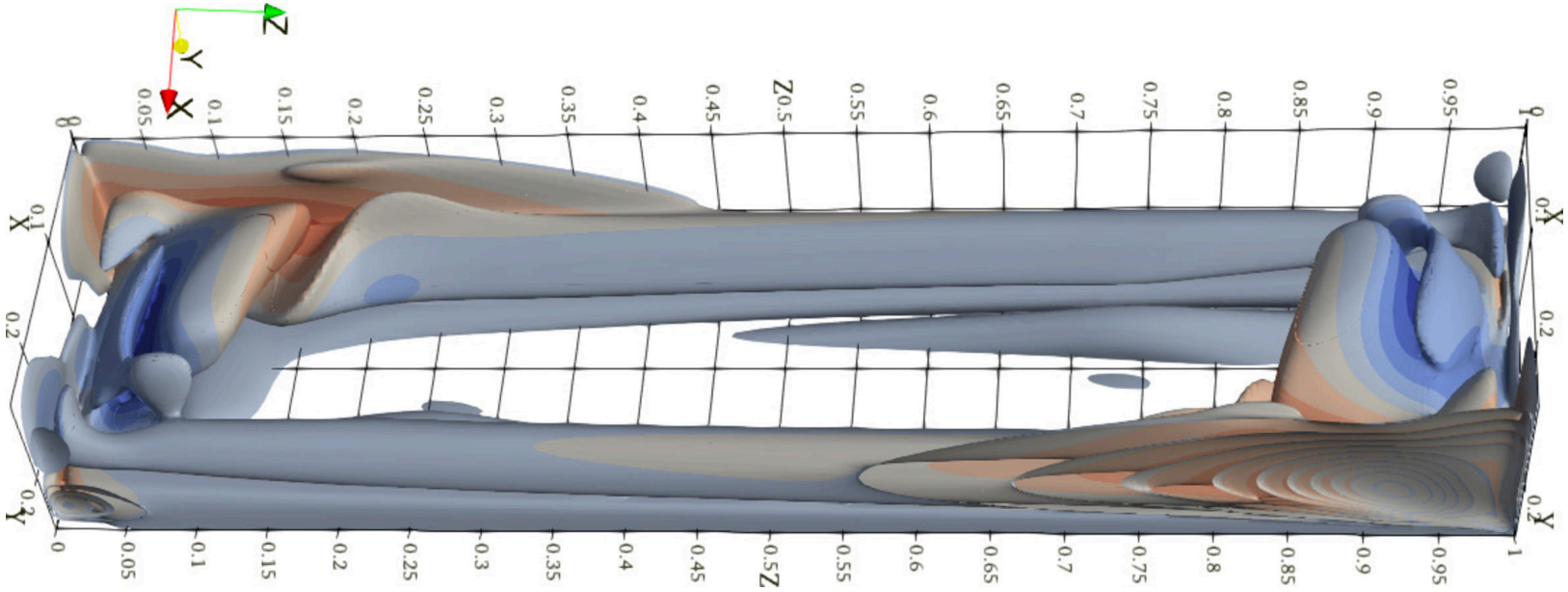

PLEASE CITE THIS ARTICLE AS DOI: 10.1063/5.0100218

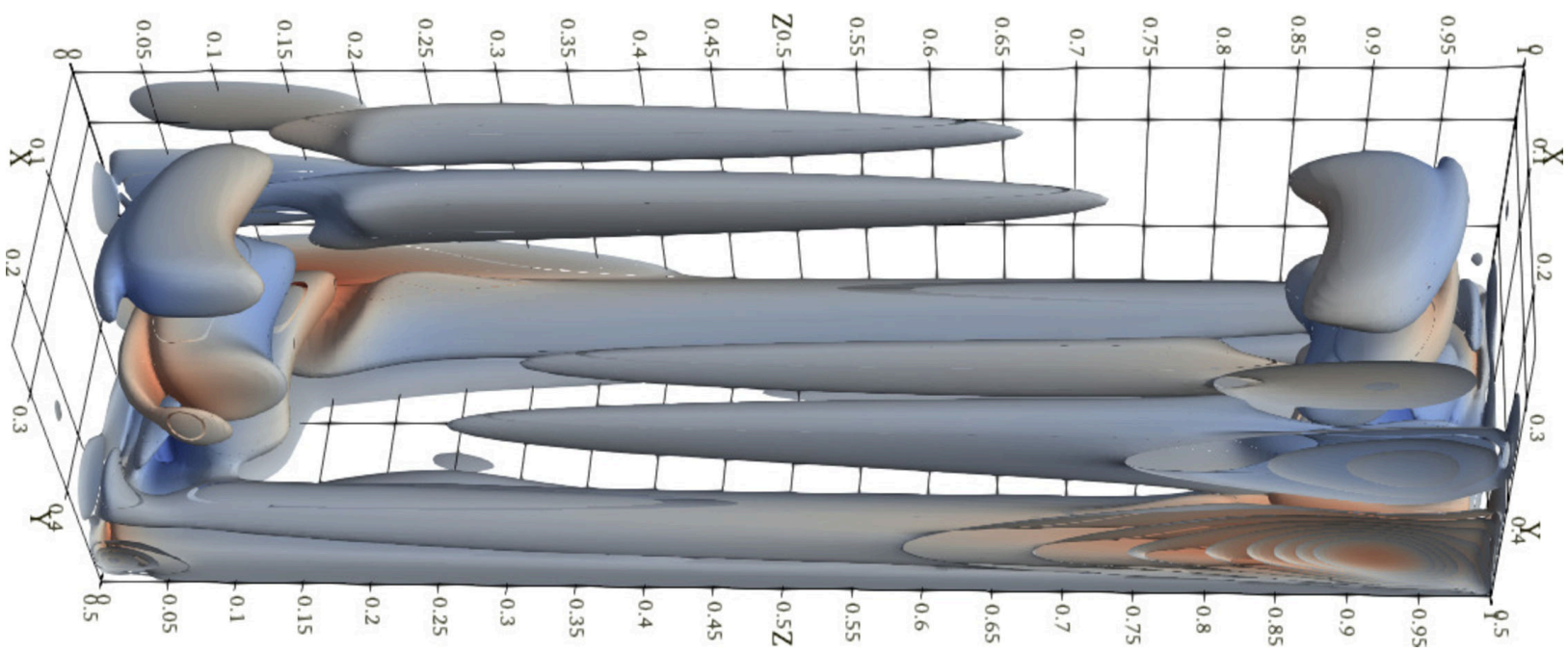

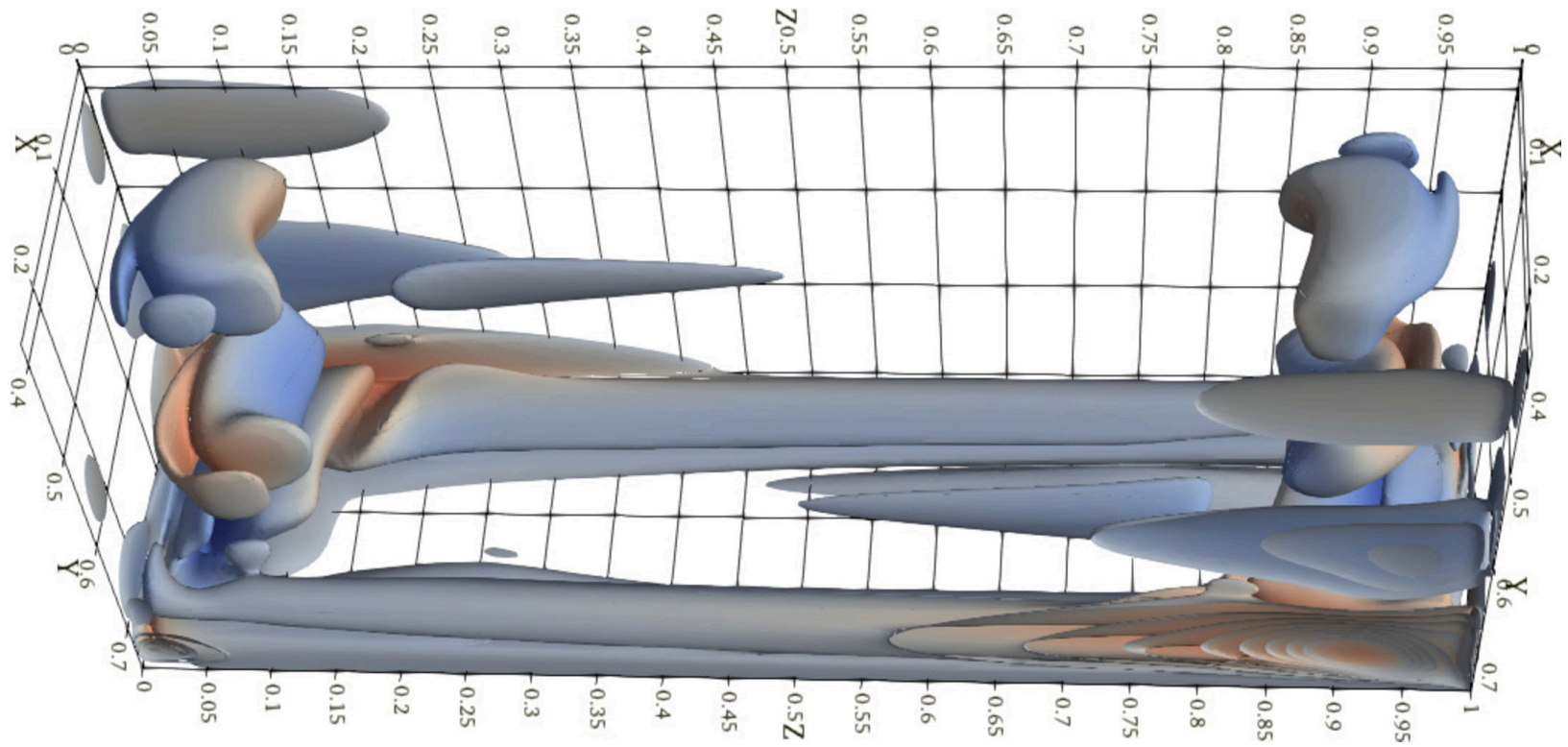

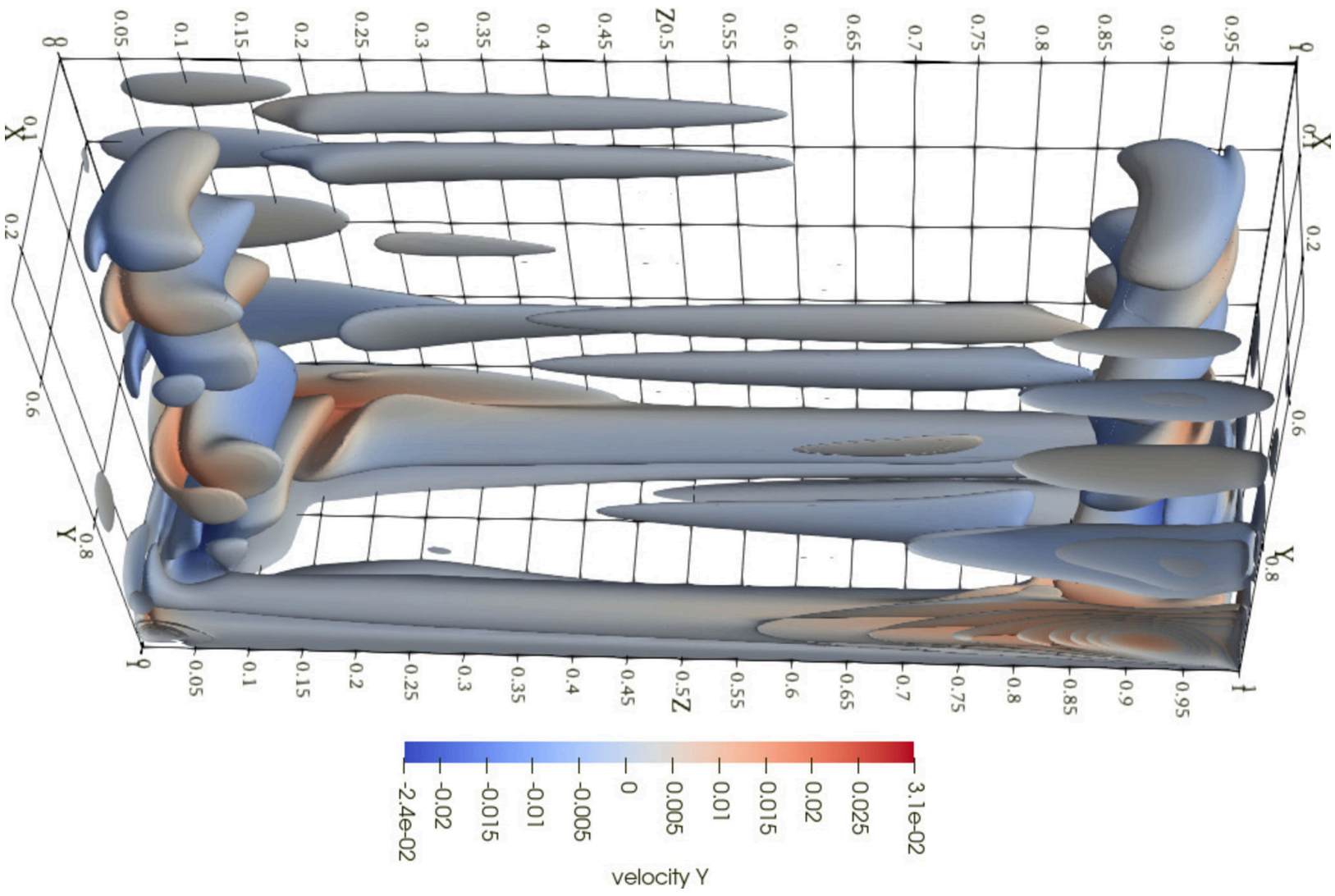

PLEASE CITE THIS ARTICLE AS DOI: 10.1063/5.0100218

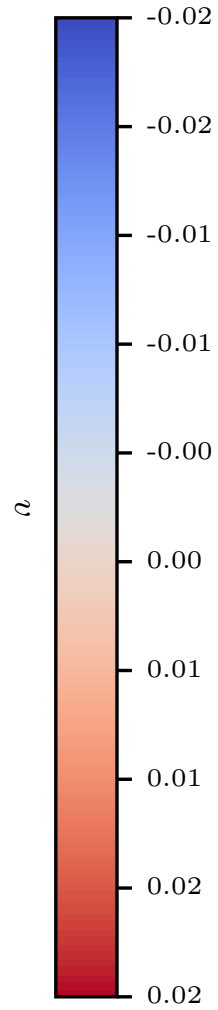

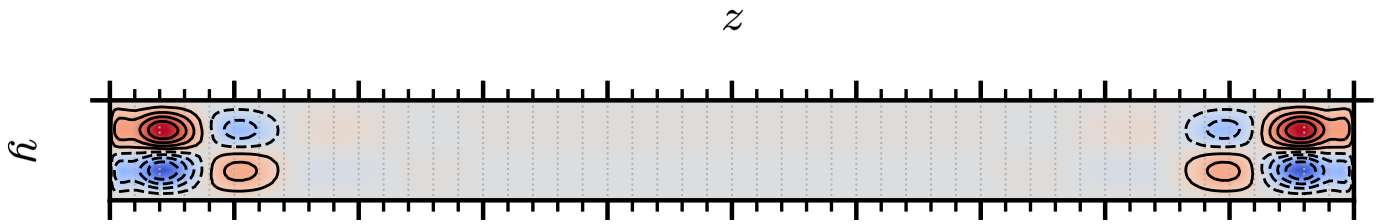

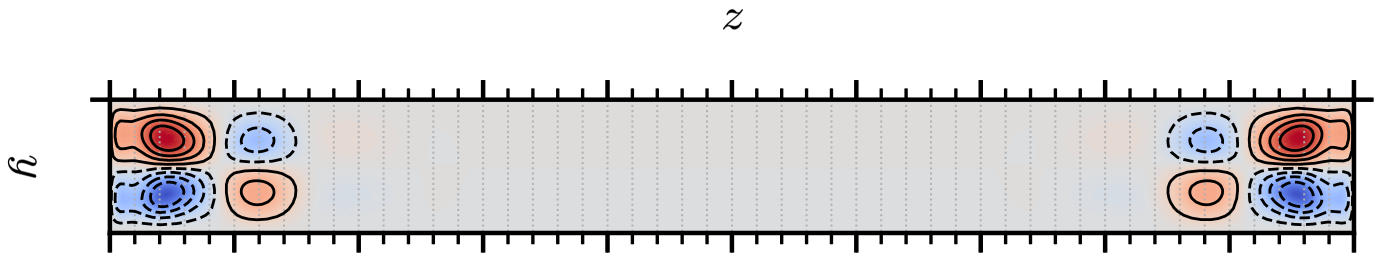

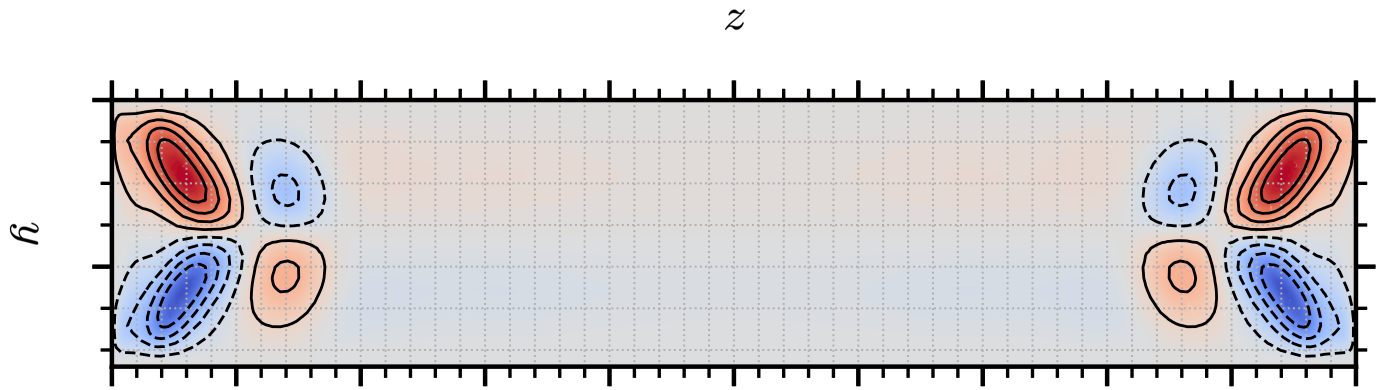

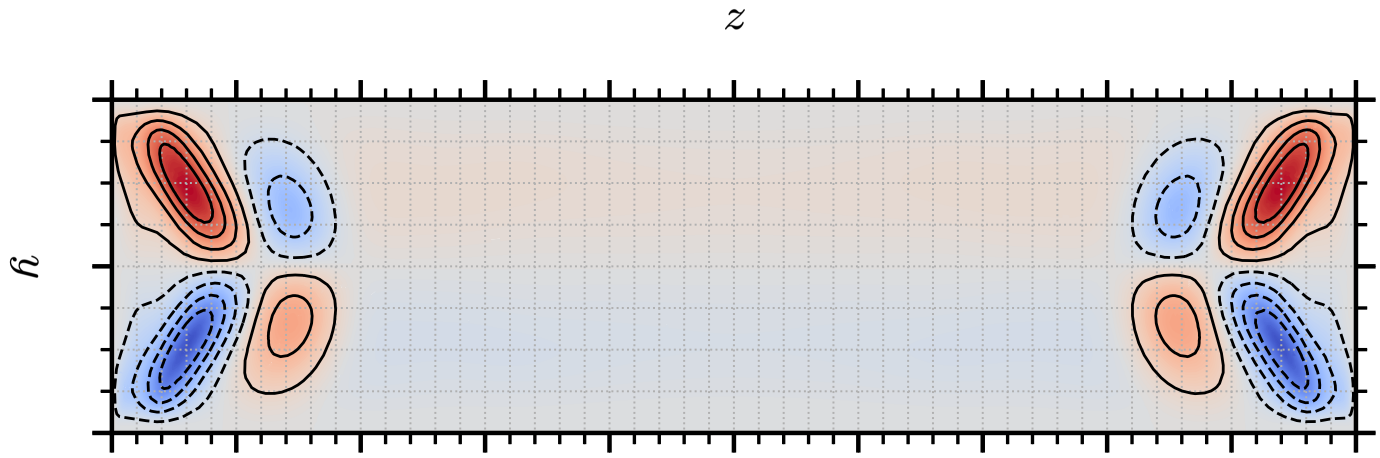

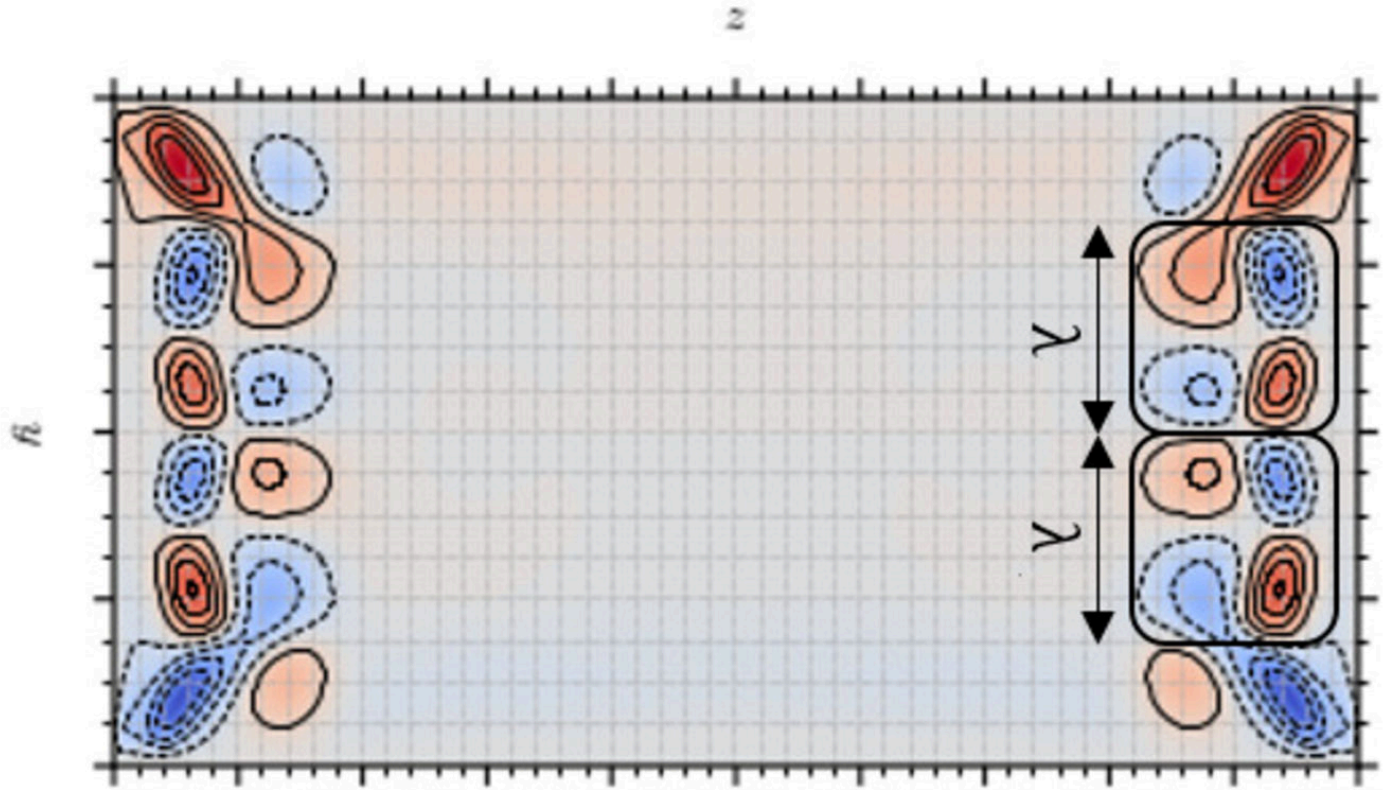

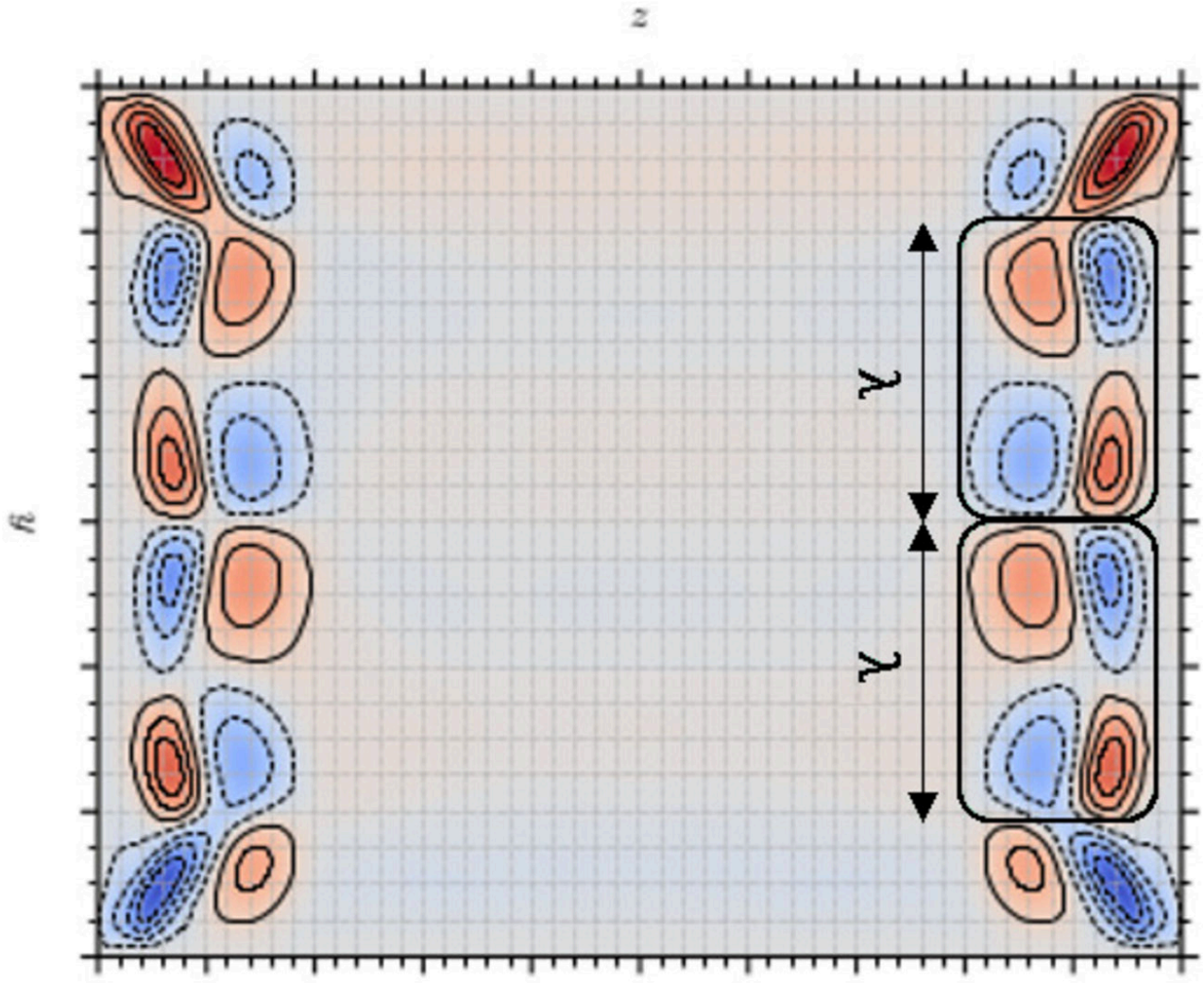

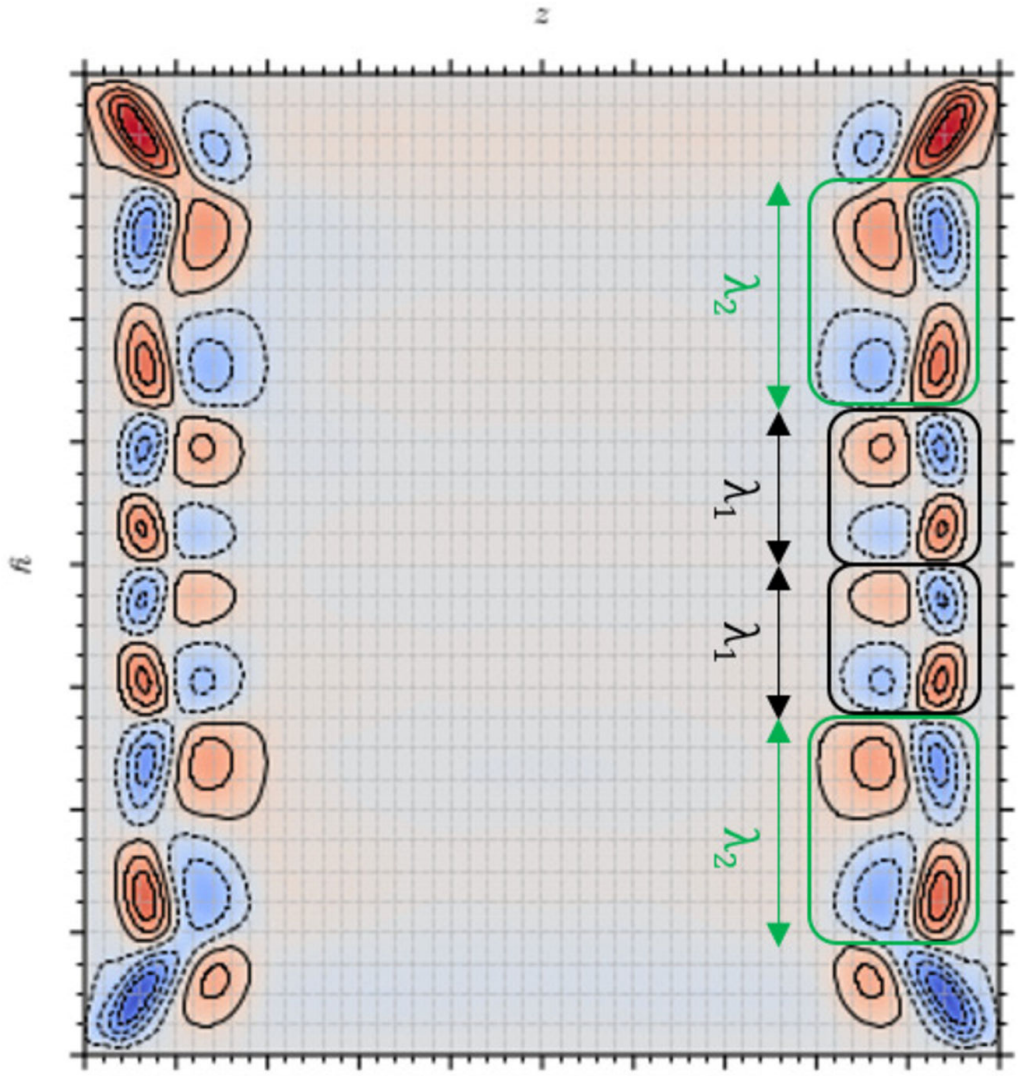

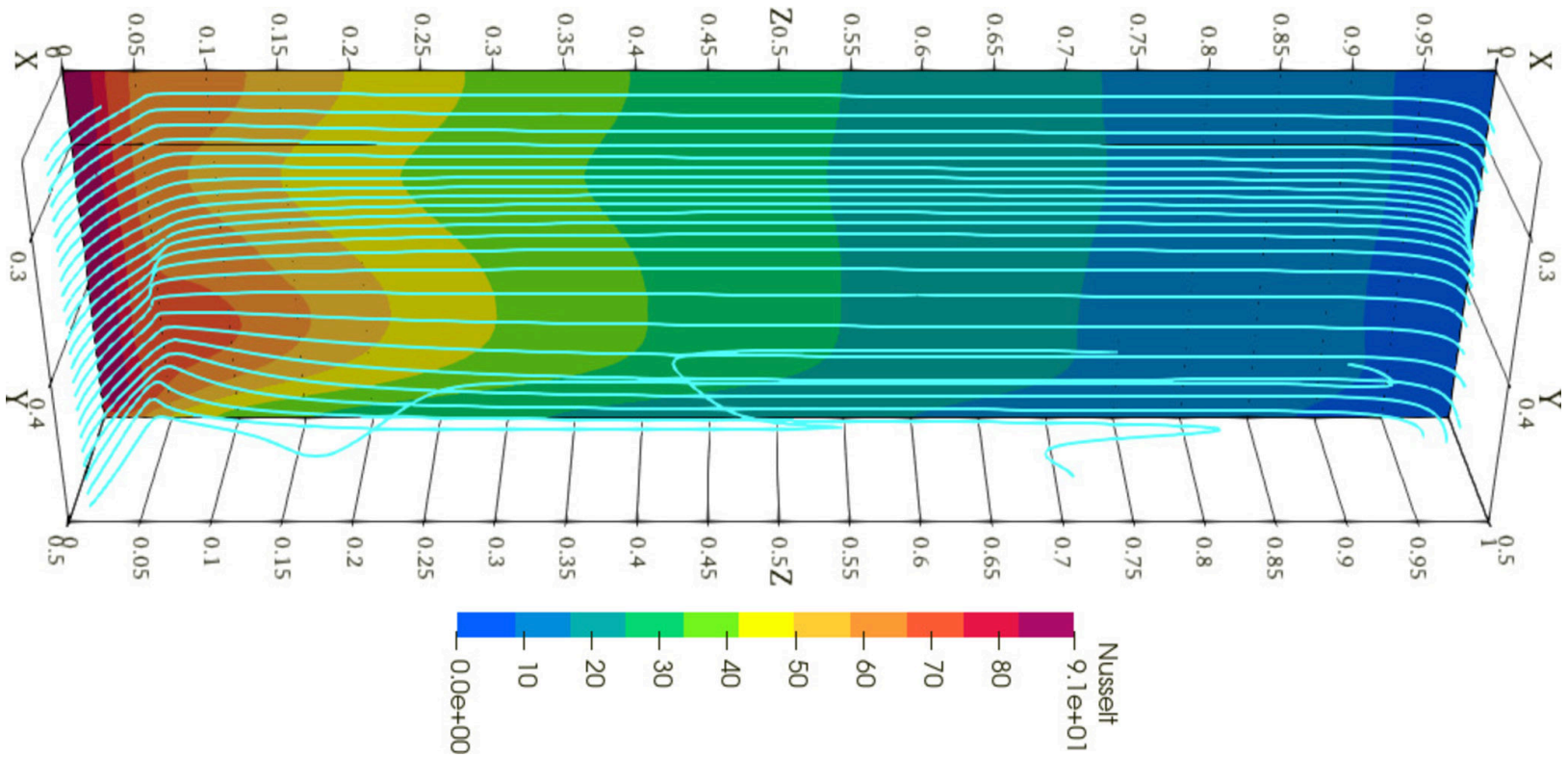

PLEASE CITE THIS ARTICLE AS DOI: 10.1063/5.0100218

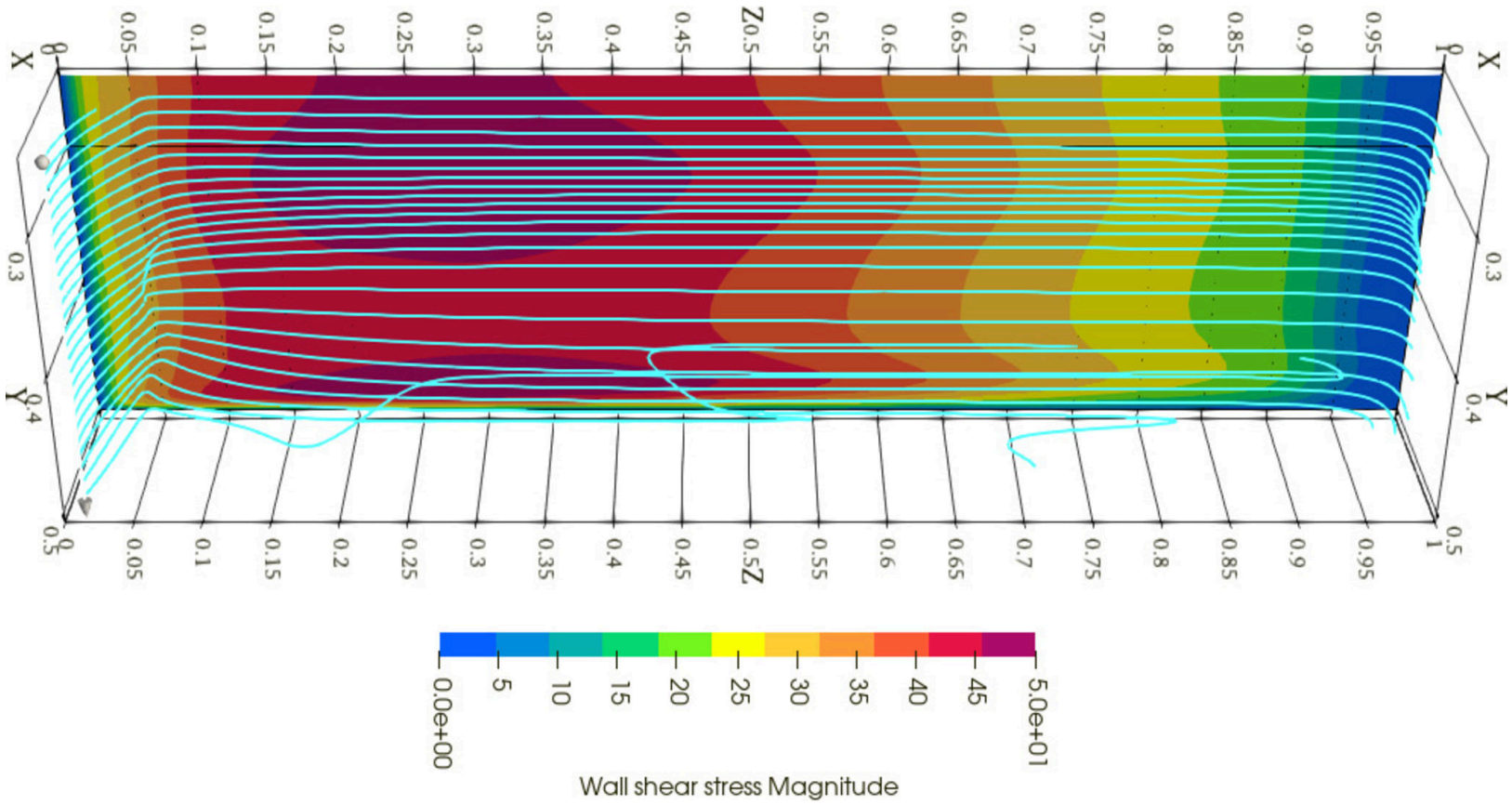

Physics of Fluids

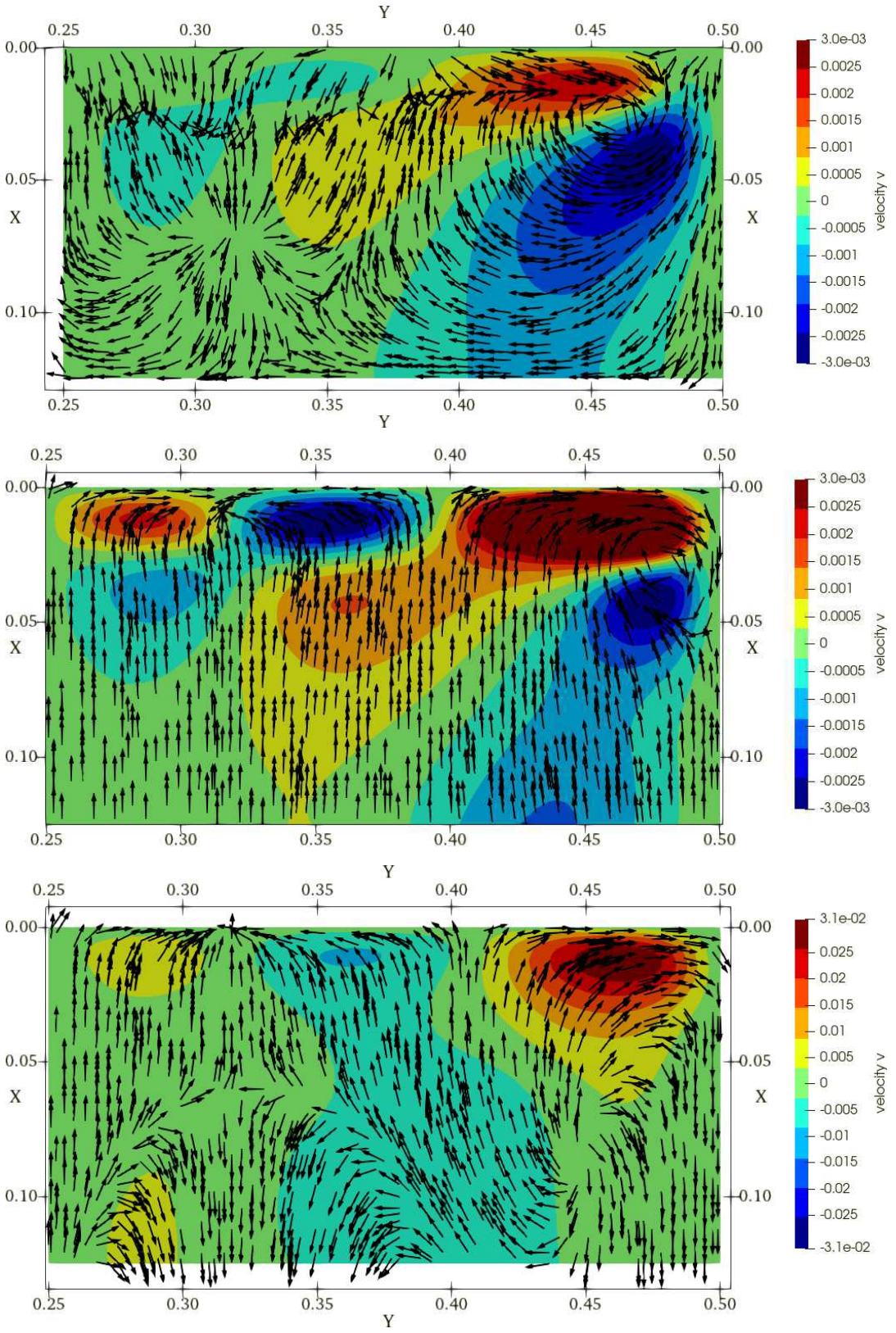

Accepted to Phys. Fluids 10.1063/5.0100218

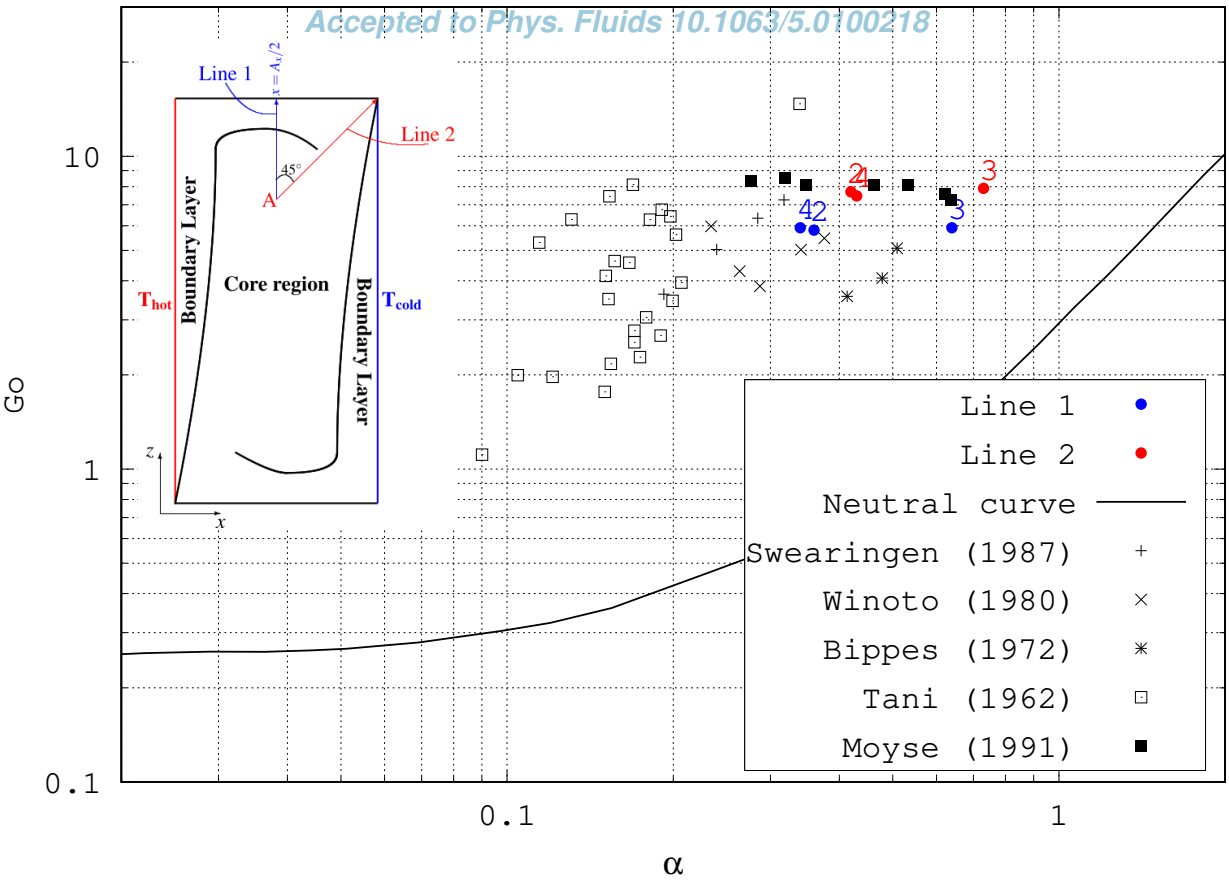

PLEASE CITE THIS ARTICLE AS DOI: 10.1063/5.0100218